Mineralogy and Petrology
https://doi.org/10.1007/s00710-026-00972-2

RESEARCH

Trace element mass transfer during the retrogression of biotite and cordierite

Elisa Oliveira da Costa[1] · Leo M. Kriegsman[2,3] · Barbara E. Kunz[1] · Clare J. Warren[1] · Tom T. Argles[1]

Received: 8 October 2025 / Accepted: 30 January 2026

Abstract
The crustal element cycle allows continuous redistribution of elements through different crustal reservoirs. Although retrogression after peak metamorphism is commonly known to affect both major and trace elements, particularly in the presence of fluids, much is still unknown about the trace element mass transfer associated with specific retrograde reactions. This study investigates the extent to which the retrograde breakdown of biotite and cordierite – key hosts of Li, Be, Cs, Sn, Ta and W in metapelites and granites – can mobilise their hosted critical elements. We combined petrography, *in-situ* mineral major and trace element analysis, bulk-rock major element analysis, geothermometry, phase equilibria modelling and mass transfer estimates to investigate the breakdown of biotite and cordierite to chlorite and pinite, respectively. The biotite to chlorite reaction (350–500 °C) requires fluid influx to produce the observed volumes of chlorite, muscovite, ilmenite, and rutile. This reaction results in substantial mobilisation of Cs and moderate losses of Li and Sn, while W, Nb, and Ta remain relatively immobile. Cordierite breaks down below ~200 °C into fine-grained aggregates of kaolinite and smectite clays (known as pinite), with element mobilisation varying with the degree of replacement, fluid composition and clay mineralogy. Li, Be, and Cs show contrasting behaviours, with mobilisation enhanced in Fe- and Mg-poor clays under open-system conditions. Our findings highlight that the breakdown of biotite and cordierite releases critical elements stored in these phases, which could potentially generate enriched fluids.

Keywords Mass transfer · Retrogression · Cordierite · Biotite · Fluids

Introduction

A fundamental knowledge of the reactions that allow chemical elements to be transferred between crustal reservoirs is essential for understanding a whole range of processes from the distribution of resources to impacts on the hydro- and biosphere. As rocks experience changes in pressure and temperature, their mineralogy changes in response. During prograde metamorphism, more hydrated minerals are progressively replaced by less hydrated minerals, with hydrous fluids released into the local environment. During retrograde metamorphism, higher-grade anhydrous minerals react with fluids to generate new hydrated minerals that are more stable under the ambient conditions (e.g., sericitization of feldspars, pinitisation of cordierite, chloritization of biotite – e.g., Putnis 2021; Yardley et al. 2014). Due to the involvement of fluids, retrograde reactions are a strong candidate for mobilising trace elements from metamorphic and igneous rocks at upper crustal levels.

Recrystallisation in the presence of fluids involves the partitioning of elements between the minerals and the fluid, and the fluid has the potential to mobilise these elements, causing them to be removed from the system (Putnis 2021). For instance, light rare-earth elements are transferred to the fluid phase during the replacement of calcic plagioclase by albite in the presence of a saline solution (Hövelmann et al.

Editorial handling: N. Cheng

✉ Elisa Oliveira da Costa
elisa.oliveira.da.costa@gmail.com

[1] School of Environment, Earth and Ecosystem Sciences, The Open University, Walton Hall, Milton Keynes MK7 6AA, UK

[2] Department of Research and Education, Naturalis Biodiversity Center, Darwinweg 2, Leiden 2333 CR, Netherlands

[3] Department of Earth Sciences, University of Utrecht, Princetonlaan 8A, Utrecht 3584 CB, Netherlands

Published online: 20 February 2026

2010). Experimental studies have widely demonstrated that fluid-mineral partitioning is dependent on physicochemical parameters such as temperature, fluid composition and acidity (e.g., Ji et al. 2021; Osvald et al. 2018; Yang et al. 2023; Yuan et al. 2021). Nevertheless, the mobilisation of trace elements will also depend on the minerals involved in the retrograde reaction, since the breakdown of mineral hosts of any trace element will only release these elements to the fluid if the solid mineral products of the reaction do not immediately sequester them. For example, biotite breakdown reactions mobilise Nb differently depending on the mineral products of the reactions (Yang et al. 2023), and garnet breakdown involves the mobilisation of different major and trace elements depending on the products formed (Baidya et al. 2019). Despite evidence that retrograde reactions mobilise trace elements, we still lack quantitative constraints on how specific retrograde breakdown reactions do so. Consequently, the extent to which specific retrograde reactions control trace element release remains poorly constrained.

The increased demand of so-called critical elements has led to the fundamental question of how these elements are mobilised and transferred within the crust in addition to magmatic processes. Several studies have revealed that processes such as weathering and sedimentation (Romer and Kroner 2016) and prograde metamorphic reactions (Kunz et al. 2022) can affect selected elements, but their behaviour strongly depends on the presence or absence of specific mineral hosts. Here we investigate the trace element mobilisation associated with the retrograde breakdown of two critical element mineral hosts in metapelites and granites. Both biotite – one of the main hosts of Li, Sn, Cs, Ta, and W, and cordierite – one of the main hosts of Li and Be, and to a lesser extent Cs have been shown to host and influence the distributions of these elements (e.g. Bertoldi et al. 2004; Kunz et al. 2022). Importantly, retrograde alteration of both minerals is widely documented in many metamorphic terranes (e.g., chloritisation of biotite: Moine et al. 1989; Broussolle et al. 2015; Oziegbe and Oziegbe 2023; Faehnrich et al. 2023; pinitisation of cordierite: Perreault and Martignole 1988; Ludhová and Janák 1999; Ogiermann 2002; Sturm 2017; Lal 1969). Biotite commonly alters to chlorite group minerals during subsolidus retrograde metamorphism, while cordierite commonly gets selectively altered to 'pinite' (a petrographic term covering a wide range of products such as hydrous alkali-bearing phyllosilicates, muscovite-chlorite mixtures, clay mineral assemblages and even isotropic minerals; Ogiermann 2002; Walker 1993).

Our approach combines petrography and *in-situ* mineral major and trace element data of mineral products and reactants to investigate both retrograde reactions, as well as bulk-rock major analysis, geothermometry, phase equilibria modelling and mass transfer estimates. Our findings indicate that the pervasive selective alteration of biotite and cordierite can effectively release critical elements to fluids (specifically Li, Be and Cs from cordierite, and Li, Sn and W from biotite), which have the potential, under the right circumstances, to be further concentrated and precipitated to form mineral deposits.

Geological materials

We selected the well-exposed Paleozoic Variscan Orogen in Europe (Franke et al. 2021) to sample high-grade metapelites and metapsammites across different locations within the orogen, which allowed us to find good examples of the two different retrograde reactions. The seven samples (Table 1) are all from locations that record metamorphic conditions consistent with partial melting in the biotite

Table 1 Summary of pelitic migmatites used in this study. The types of pinite follow Ogiermann's (2002) classification

Area	Sample	Coordinates	Primary mineral assemblage	Degrees of pinitization and pinite-types
Tormes, SP	PT22A	41°14'35.1"N 6°36'05.2"W	Bt-Pl-Afs-Qz-Ilm-Rt-Chl-Ms	(Bt chloritization)
Mindelo, PT	PT03	41°17'54.5"N 8°44'15.1"W	Crd-Bt-Sil-Qz-Pl-Afs-Ilm-Ap	Moderate to nearly complete **m-type**
Brittany, FR	K5533	*	Grt-Crd-Bt-Qz-Pl-Sil-Ilm-Rt	Incipient f-type, **m-type**
	K5538	*	Bt-Qz-Pl-Sil-Ilm	Nearly complete b-type, **m-type**
Agly, FR	L44	42°43'38.22"N 2°34'32.41"W	Grt-Crd-Qz-Pl-Afs-Sil-Hc-Ilm	Incipient **m-type**
	L14G	42°43'14.10"N 2°36'47.72"E	Grt-Crd-Bt-Qz-Pl-Sil-Ilm-Rt	Intermediate b-type, **m-type**
	L10A	42°43'17.81"N, 2°38'28.94"E	Crd-Bt-Qz-Pl-Sil-Ilm	Nearly complete **i-type**, f-type

* Sample location described in M. Brown PhD thesis (1975)

Types in bold were analysed (m-type = mat-type; f-type = fissure-type; b-type = border-type; i-type = isotropic-type). *SP*, Spain; *PT*, Portugal; *FR*. France. Mineral abbreviations from Whitney and Evans (2010)

dehydration field (Johnson and Brown 2004; Silva 2014; Siron et al. 2020; Viruete et al. 2000). The trace element mobilisation associated with the chloritization of biotite was investigated using a psammitic metatexite with unaltered and altered bands on the scale of a single thin section (PT22A from the Tormes Gneissic Dome, Spain). The trace element mobilisation associated with the pinitization of cordierite was investigated with six metapelitic migmatites from three areas where the peritectic cordierite shows incipient to extreme alteration to either mat-type and/or isotropic-type pinites (Ogiermann 2002). A local description of the geological settings of the four different areas is provided in the Supplementary Text.

Methods

Sample collection and Preparation

Samples were either collected during fieldwork or shared by other colleagues. Samples from Brittany were shared by M. Brown, while S. Hoogendoorn and L. Kriegsman shared samples from the Agly Massif. Samples from the Moldanubian region were collected during fieldwork in November 2021, and samples from Mindelo and Tormes were collected during fieldwork in March 2022.

Thin sections with 30 and 40 µm thickness were prepared at the Open University for each sample. Thin sections with 30 µm thickness were covered by glass coverslips and were used for optical petrographic observation and photomicrographs, while 40 µm polished thin sections were used for all *in-situ* geochemical analyses described below. The 40 µm thickness minimised the potential of drilling too quickly through mineral phases into the glass below during Laser Ablation Inductively Coupled Plasma Mass Spectrometry (LA-ICP-MS) analysis without compromising optical microscopy too much. Petrographic descriptions and photomicrographs were acquired with a Hinotek XPL-3220 polarization microscope, a Leica Wild MZ8 Stereo Microscope, a GXCAM-U3PRO-6.3 microscope camera, and the GT Vision software. Mineral abbreviations are after Whitney and Evans (2010).

The preparation of powders for whole-rock analysis required the utmost attention to detail to avoid cross-contamination due to low concentrations of the trace elements relevant to this investigation. Initially, the hand specimens were crushed with a fly press to a size of 4 cm or less. To avoid contact with any metallic surfaces during the crushing process, which could introduce contamination of metals, samples were wrapped in sheets of paper and plastic bags. After initial crushing and sorting, the rock chips were washed and ultrasonicated in milli-Q water for 5 min and then dried at 40 °C in an oven overnight. Finally, samples were crushed in a Siebtechnik/Tema agate disk mill to clay and/or silt grain size. Between samples, the disk mill vessel was cleaned with ethanol, followed by a 2-minute cycle of pure quartz milling and another ethanol clean. During all steps, samples only touched surfaces covered in paper, which was changed between each sample.

Bulk rock geochemistry

Bulk-rock major elements composition and trace element concentrations were acquired at the Activation Laboratories (Canada). Analyses in ALS Global in Canada were carried out using the analytical package ME-MS71-L, which analyses major elements using fusion-Inductively Coupled Plasma (ICP) and trace elements using by ICP-Mass Spectrometry (ICP-MS) using lithium tetraborate/metaborate fusion. Samples were analysed in a batch system containing a method reagent blank, a certified reference material and 6 replicates of different samples. Calibrations are performed using one of the fourteen United States Geological Survey (USGS) and Canada Centre for Mineral and Energy Technology (CANMET) certified reference materials, analysed between every 10 unknown samples. Acceptable totals are between 98.5% and 101%. Lower results could indicate the presence of base metals, sulphate, or Li, which have not been analysed, but that was not observed in my samples. Detection limits for Al_2O_3, CaO, Fe_2O_3, K_2O, MgO, Na_2O, P_2O_5, SiO_2 and loss on ignition are 0.01 wt%, while for MnO and TiO_2 are 0.001 wt%. Seven standards were used verify the data quality of major elements, and the results were within 7% of the preferred values. When considering only the standards chemically closest to metapelitic migmatites (GBW07113: rhyolite; SY-4: dioritic gneiss), results were within 5% of the preferred values. For trace elements, detection limits are typically below 1 ppm. Thirteen standards were used to verify the data quality of trace element analysis, and results were typically within 10% of the preferred values, with rare exceptions within 20% of the preferred values. Results within 20% of the preferred values are not a problem since these results occur for only one of the standards, while the other standards are with 10% of the preferred values for the same element. Duplicate analysis of sample N34 normally shows 21 up to 10% differences, except for Tl, Tm, Tb, As and Ni, which vary up to 20%. Blank results are all below detection limits. The results are shown in Electronic Supplementary Material 2.1, and the detection limits and data quality checks are in Electronic Supplementary Material 1.2.

In-situ major element analysis

In-situ major element compositions for cordierite, pinite, biotite, chlorite, muscovite and feldspars were acquired at the Open University, England, using both the Tescan Clara Energy-Dispersive Spectroscopy Scanning Electron Microscope (EDS-SEM) with beam conditions of 20 keV and 3 nA and a Cameca SX100 (five wavelength dispersive spectrometer EPMA) with an unfocused beam and column conditions of 20 keV, 20 nA. Data quality of EDS-SEM semi-quantitative analysis was checked by the analysis of a natural almandine standard from the GEO MkII block made by PandH Developments Ltd, which was analysed at the beginning and end of sessions and lay within 7% of the standard preferred values. For the EPMA, elements were acquired using LPET for Ca and Ti, LPET for Cl, K, and Cr, LLIF for Fe and Mn, TAP for Si and Mg, and LTAP for F, Na, and Al. The ZAF correction was conducted using X-PHI. In-house garnet and amphibole standards are run x3 at the start of every analytical session to check accuracy and precision of major elements; the achieved net analytical uncertainty was between 1.5 and 2% on all major elements, usually slightly higher for Mn and Cr, around 3–4%, and detection limits were up to 0.03 wt% for most oxides with the exception of Cr2O3, which had detection limits of 0.12 wt%. Analyses of rutile and ilmenite were acquired using a JEOL 5-spectrometer JXA-8530 F (EPMA) at the University of Utrecht, Netherlands, with 2 µm beam and column conditions of 50 keV and 20 nA. Elements were acquired using LIFH for Fe, Mn, Ta, PETL for Cr, Nb, Ti, PETH for Ca, K, Zr, PETL for Cr, Nb, Ti, TAP for Si, Al, TAPH for Mg, Na, TAP for Si, Al, and TAPH for Mg, Na. Data quality was verified by R10 standard measurements (Luvizzotto et al. 2009) at the beginning and end of the session. Relative standard deviations range from 0.9 to 2.5% for Ti, Cr, Fe, Nb and Zr, and 13% for Ta, and detection limits ranged from 0.002 to 0.011 wt%. Off-peak correction method was linear for Ti, Fe, Mn, Na, K, and exponential for Al, Mg, Ca, Cr, Si, Zr, Nb, Ta. Unknown and standard intensities were corrected for deadtime, and interference corrections were applied to Si for interference by Ta, Nb, and to Mn for interference by Cr. Metadata associated with EPMA analysis is shown in Electronic Supplementary Material 1.3, and data quality checks for EDS-SEM are shown in Electronic Supplementary Material 1.4.

In-situ trace element analysis

In-situ mineral trace element concentrations of individual mineral grains were acquired using a Photon Machines Analyte G2 193 nm excimer laser system equipped with a HelEX II laser ablation cell coupled to an Agilent 8800 Triple Quadrupole ICP-MS (LA-ICP-MS) at the Open University, England. Before analysis, the instrument was tuned using the SRM-NIST 612 glass to optimise ICP-MS sensitivity and reduce oxide production (<0.1%). Analytical conditions for biotite, muscovite, chlorite, feldspars, cordierite and pinite consisted of a laser fluence of 3.63 J/cm^2, 10 Hz repetition rate, 50–30 µm spot size, 30 s gas blank, 30 s ablation, and 40 s gas washout; while analytical conditions for the analysed of ilmenite and rutile consisted of a laser fluence of 3.63 J/cm2, 5 Hz repetition rate, 20 µm spot size, 30 s gas blank, 30 s ablation, and 50 s gas washout. SRM-NIST 612 glass was used as a primary standard and BCR-2G as the secondary standard for silicate analyses. SRM-NIST 610 glass was used as a primary standard and R10 rutile (Luvizotto et al. 2009) was used as a secondary standard for the Ti oxide analyses. Primary and secondary standards were analysed at the start and end of every run and between every 20–30 unknowns. Detection limits of trace elements are typically between 0.1 and 1 ppm. Data reduction was carried out using Iolite v3.71 (Paton et al. 2011) applying the TraceElement_IS data reduction protocol with ^{29}Si as the internal standard for the silicates and ^{49}Ti for ilmenite and rutile (using the SEM and/or EPMA analyses). The quality of the analysis was evaluated by BCR-2G and R10, which typically were within 10% of the published value. Operating conditions and detection limits are shown in detail in the Electronic Supplementary Material 1.5, and data quality checks are shown in Electronic Supplementary Material 1.6. *In-situ* major and trace elements results for chloritization and pinitization are shown in Electronic Supplementary Materials 2.1 and 2.2, respectively.

Thermodynamic and geochemical modelling

Pressure and temperature estimates for sample PT22A were calculated to confirm that biotite in the fresh domain is representative of the reactant of the retrogressive reaction and not in equilibrium with the minerals in the altered domain. The pressure and temperature conditions for this sample were constrained using the chlorite (Lanari et al. 2014), Zr in rutile (Watson et al. 2006), and Ti in biotite (Wu and Chen 2015) geothermometers as well as by phase equilibria modelling using the software GeoPS (Xiang and Connolly 2022) with the thermodynamic dataset hp622ver.dat (Holland and Powell 2011; as used in Jennings and Holland 2015). Solution models for white mica, biotite, ilmenite, chlorite and melt were sourced from White et al. (2014), while the model of Fuhrman and Lindsley (1988) was used for feldspar. Phase equilibria modelling of sample PT22A used whole-rock compositions, which were recalculated to account for the water contents of the fresh and altered domains and isopleths based on mineral chemistry. Pressure and temperature diagrams of fresh and altered domains in sample PT22A were used to constrain P-T

conditions, and T-X (varying H_2O content) plots were used to estimate the amount of water necessary to reach the observed proportion of chlorite in the thin section. Some phases from the solution models for staurolite (fst), aluminosilicates (sill, ky, and), corundum (cor), and garnet (spss, alm) were excluded because (1) these phases were not observed in thin section; (2) inclusion resulted in many small, possibly metastable, stability fields, and (3) very similar results were generated including and excluding these end members.

The biotite-to-chlorite reaction stoichiometry was determined by solving a set of linear equations for each of the system components on a molar basis, using linear algebra in an Excel spreadsheet and an approach similar to that described in Thompson (1982). System components corresponded to the minimum set of oxides needed to characterise the composition of key phases involved. Average atoms per formula unit of the phases were used in the calculations. Stoichiometry calculations are provided in the Electronic Supplementary Material 2.3. The reaction products were normalised to biotite whose reaction coefficient therefore equals 1. Mass transfer associated with the chloritization of biotite was calculated using the proportions of mineral products of the reaction and minimum, maximum, and average trace element concentrations of the minerals. The proportion of mineral products was calculated by two approaches: (1) stoichiometric – mineral chemistry was used to calculate the reaction's stoichiometry; molar proportions of the reaction products were subsequently converted to weight and normalised to the molar weight of biotite; (2) visual – reaction product proportions were obtained from the compositional maps of the altered domain and normalised to 100%.

Results

Petrography and mineral chemistry

Sample PT22A consists of continuous millimetric leucocratic and melanocratic bands. Some domains in the sample contain fresher biotite (bottom of Fig. 1a); others have more altered biotite (middle to top of Fig. 1a). In the "fresh" domains, leucocratic bands are composed of quartz and feldspars, while melanocratic bands contain biotite, minor chlorite and muscovite, and accessory ilmenite and rutile (Figs. 1d, e). In altered domains, plagioclase crystals are strongly sericitized and biotite crystals are completely replaced by chlorite and muscovite with more numerous and larger Ti-oxide inclusions (Figs. 1b, c). Major element compositions of biotite, chlorite, muscovite, plagioclase, K-feldspar, rutile, and ilmenite in Sample PT22A are in Table 2, and the average mineral formulae for the main minerals in the reaction are provided in Table 3.

The best-fitted stoichiometry of the observed biotite-replacing reaction:

$$\mathrm{Bt} + \mathrm{H_2O} = \mathrm{Chl} + \mathrm{Ms} + \mathrm{Ilm} + \mathrm{Rut} + \mathrm{K_2O} \quad (1)$$

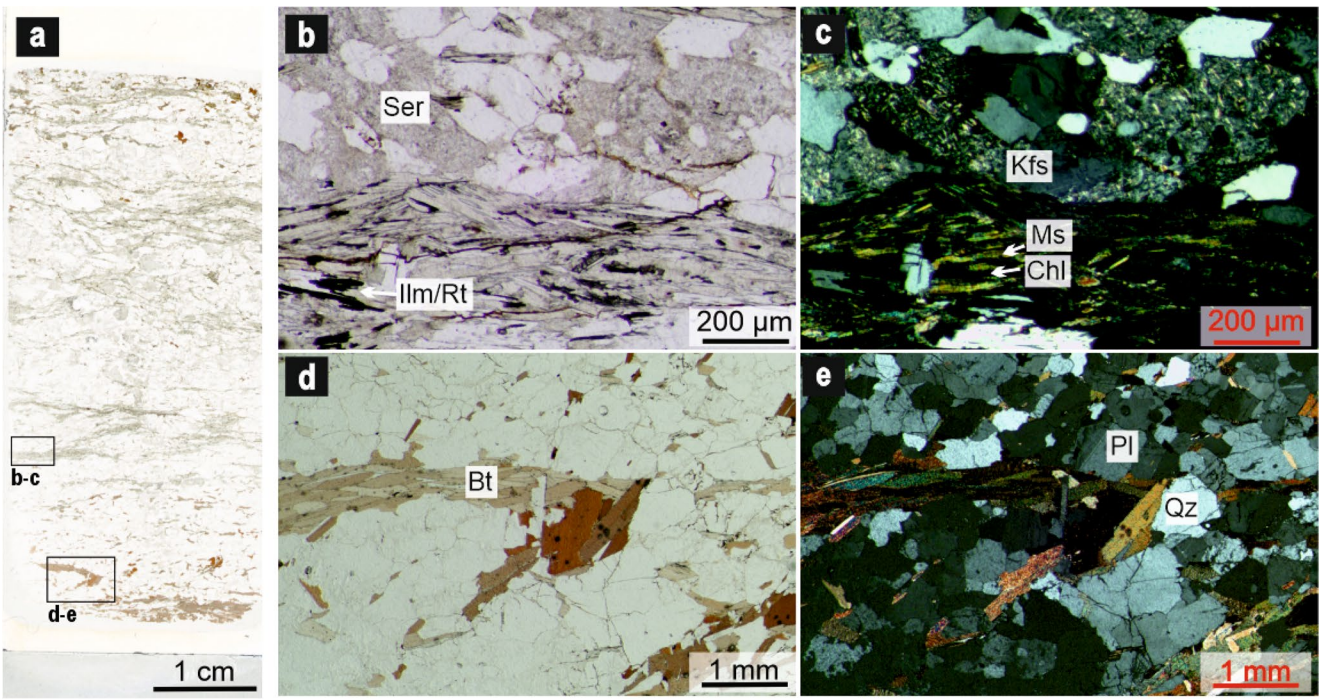

Fig. 1 **a** Thin section scan of sample PT22A with locations of subsequent photomicrographs **b**–**e** indicated. **b**, **c** Photomicrographs of an altered area under plane and crossed polarised light. **d**, **e** Photomicrographs of the fresh area under plane and crossed polarised light

Table 2 Representative chemical compositions of minerals in sample PT22A X_{Fe} = (Fe/[Fe + Mg]), X_{Mg} = (Mg/[Fe + Mg]), X_{An} = (Ca/[Ca + Na + K]), X_{Ab} = (Na/[Ca + Na + K]), and X_{Or} = (K/[Ca + Na + K])

Oxide (wt%)	Detection Limits	Biotite	Muscovite	Chlorite	Plagioclase	Alkali-feldspar	Ilmenite	Rutile
SiO_2	0.002	35.64	45.48	25.29	61.87	64.16	0.19	0.43
TiO_2	0.02	3.01	0.69	0.08	-	0.02	51.59	96.86
Al_2O_3	0.016	19.74	37.23	22.55	24.95	18.88	0.00	0.17
Cr_2O_3	0.12	-	-	-	-	-	-	-
FeO	0.05	19.68	0.99	28.01	-	-	42.75	0.67
MnO	0.07	0.23	-	0.28	-	-	3.13	-
MgO	0.016	8.10	0.51	12.27	-	-	-	-
CaO	0.006	-	-	0.01	5.53	0.01	-	0.14
K_2O	0.024	9.30	10.40	-	0.35	15.18	-	-
Na_2O	0.024	-	0.43	-	8.39	0.68	-	-
ZrO_2	0.005						0.007	0.010
Nb_2O_5	0.006						0.087	0.269
Ta_2O_5	0.010						-	0.022
Atoms per formula unit (apfu)		11 O	11 O	14 O	32 O	32 O	3 O	2 O
Si		2.69	3.00	2.67	10.87	11.93	0.00	0.01
Ti		0.17	0.03	0.01	0.00	0.00	1	0.98
Al^{IV}		1.31	1.89	1.33	5.17	4.14	0.00	0.00
Al^{VI}		0.43	0.99	1.48	5.17	4.14	0.00	0.00
Cr		0.01	0.00	0.00	0.00	0.00	0.00	0.00
Fe		1.24	0.05	2.47	0.00	0.00	0.92	0.01
Mn		0.01	0.00	0.03	0.00	0.00	0.07	0.00
Mg		0.91	0.05	1.93	0.00	0.00	0.00	0.00
Ca		0.00	0.00	0.00	1.04	0.00	0.00	0.00
K		0.9	0.88	0.00	0.08	3.6	0.00	0.00
Na		0.03	0.06	0.00	2.86	0.25	0.00	0.00
Zr							0.0001	0.00
Nb							0.0010	0.0022
Ta							0.00	0.0001

Dashes indicate analyses below the detection limit, and blanks indicate the element was not analysed. Complete results are shown in the Electronic Supplementary Material 2.1

Table 3 The average mineral formula for minerals reacting in sample PT22A

Mineral	Average formula
Biotite	$K_{0.9}$, $Na_{0.03}(Mg_{0.9}$, $Fe_{1.27}$, $Ti_{0.18}$, $Al_{0.43})[Al_{1.32}$, $Si_{2.68}$, $O_{10}](OH)_2$
Chlorite	$(Fe_{2.4}$, $Mg_{1.88}$, $Ti_{0.01}$, $Mn_{0.03}$, $Al_{1.46})[Al_{1.31}$, $Si_{2.69}$, $O_{10}](OH)_8$
Muscovite	$K_{0.88}$, $Na_{0.06}(Al_{1.85}$, $Ti_{0.05})$ $[Si_{3.04}$, $Al_{0.96}$, $O_{10}](OH)_2$
Ilmenite	$(Fe_{0.92}$, $Mn_{0.08}$, $Ti_1)O_3$
Rutile	TiO_2

Using the average molar formula for each mineral in sample PT22A is:

$$1\ \mathrm{Bt} + 0.96\ \mathrm{H_2O} = 0.17\ \mathrm{Ms} + 0.47\ \mathrm{Chl} + 0.09\ \mathrm{Ilm} + 0.08\ \mathrm{Rut} + 0.9\ \mathrm{Qz} + 0.75\ \mathrm{K_2O} \quad (2)$$

Sample L44 is a granulite with incipient pinitization of cordierite restricted to the borders of cordierite crystals, while other minerals show no alteration. The pinites are fine-grained and have low birefringence, classifying them as mat-type pinites (Ogiermann 2002). The sample leucocratic bands are composed of plagioclase, quartz and alkali-feldspar and melanocratic bands composed of garnet, cordierite, plagioclase, sillimanite and hercynite.

Sample K5533 is a diatexite with incipient pinitization similar to sample L44 (mat-type pinites), as well as fissure-type pinites observed in thin sections but not visible on the EDS maps. The sample leucosome is composed of plagioclase, quartz and cordierite, with rafts of melanosome composed of garnet surrounded by cordierite and biotite, and minor sillimanite.

Sample PT03 is a metatexite with intermediate pinitization of cordierite. In sample PT03, most cordierite crystals without inclusions are almost completely pinitized (Fig. 2a), while crystals with sillimanite and/or fibrolite inclusions have a fresh core (Fig. 2b). Pinite in PT03 is fine-grained and displays low birefringence (mat-type, Ogiermann 2002). The sample leucocratic bands are composed of quartz, plagioclase, alkali-feldspar and pinitized cordierite

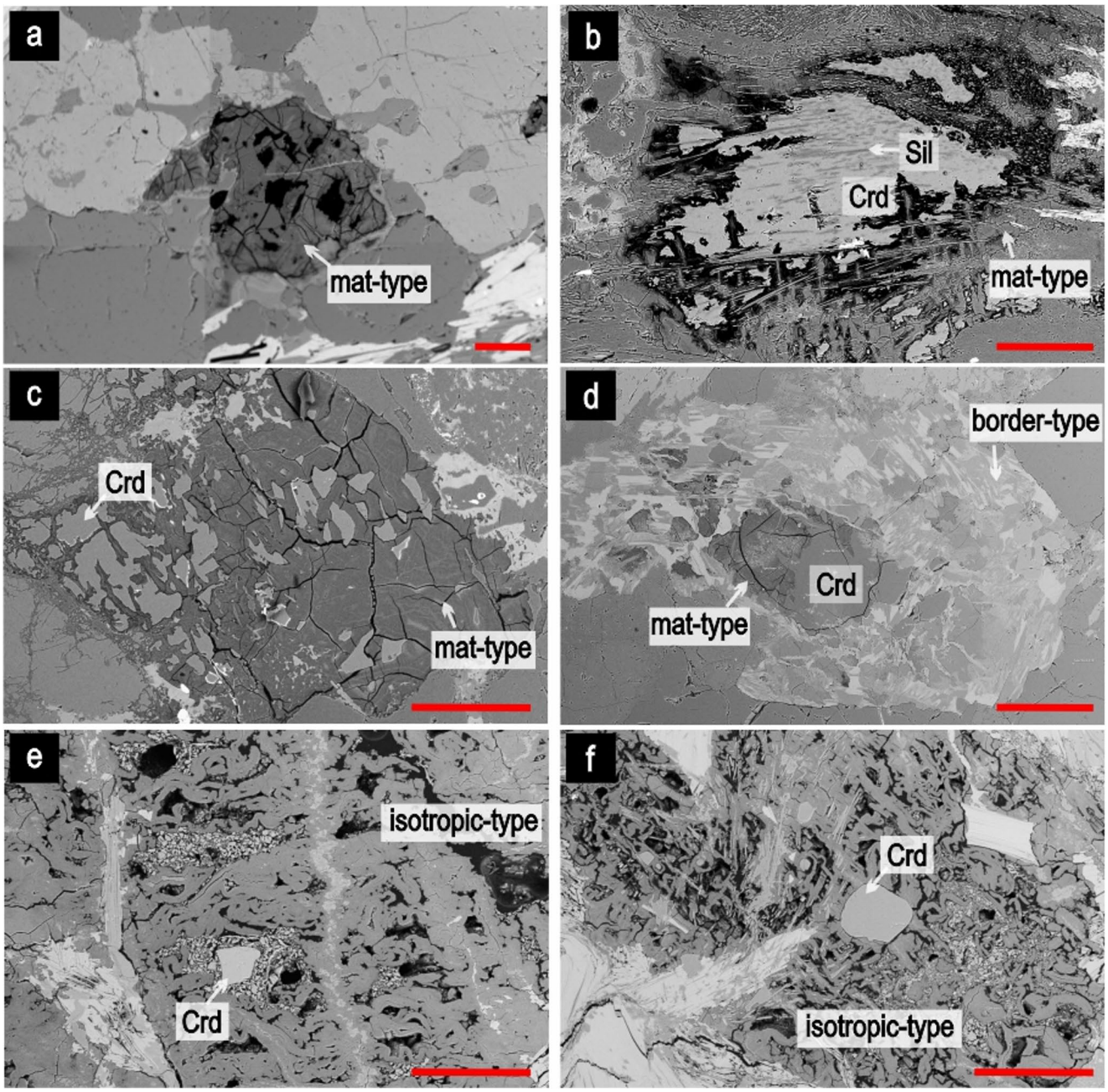

Fig. 2 Backscattered electron-SEM images of pinite types observed in samples. **a** Sample PT03 mat-type pinites completely replacing cordierite crystals without inclusions. **b** Sample PT03 mat-type pinites moderately replacing cordierite crystals with sillimanite/fibrolite inclusions. **c** Example of a larger cordierite crystal in sample L14G, partially replaced by mat-type pinite. **d** Cordierite crystal in sample K5538 nearly completely replaced by border- and mat-type pinite. **e**, **f** Sample L10A fissure- and isotropic-type pinite nearly completely replacing cordierite. Red scale bars represent 250 µm

with fibrolite inclusions, while melanocratic bands are composed primarily of biotite and cordierite. Besides cordierite, other minerals are unaltered.

Sample L14G is a diatexite with intermediate pinitization of cordierite. In sample L14G, smaller cordierite grains are usually completely pinitized, while larger grains are moderately pinitized (Fig. 2c). Pinites are mostly mat-type, with minor border-type also present (Ogiermann 2002). The sample comprises garnet, pinitized cordierite, plagioclase, quartz, siliminate, and hercynite. Other minerals in sample L14G display higher temperature alteration and/or deformation textures, such as dynamic recrystallisation (grain boundary migration), garnet fractures filled with chlorite, and sericitization of plagioclase.

Sample K5538 is a metatexite with nearly complete pinitization of cordierite. The thin section of sample K5538

contains a single cordierite grain in the leucosome, which displays border-type pinite (petrographically distinguishable intergrowths of muscovite and chlorite) and mat-type pinite (Fig. 2d; Ogiermann 2002). The leucosome is composed of quartz, plagioclase and alkali-feldspar, while the melanosome is primarily composed of biotite.

Sample L10A is a metatexite with nearly complete pinitization of cordierite. In this sample, pinite is mostly isotropic-type, but fissure-type pinite is also present (Figs. 2e, f). Leucocratic bands are composed of plagioclase, quartz and cordierite, while melanocratic bands are composed of biotite, sillimanite and cordierite. Other minerals show evidence of higher temperature alteration and/or deformation, such as dynamic recrystallisation textures (grain boundary migration and bulging) and sericitization of plagioclase.

Table 4 summarises pinite and cordierite compositions. As the *in-situ* major element mineral analyses yielded results that indicate kaolinite-group minerals make up the pinite, the atoms per formula unit were calculated assuming 14 oxygens (as in Deer et al. 2013). Figure 3 highlights the difference between pinite compositions and the average cordierite composition in each sample.

Table 4 Representative major element compositional ranges of cordierite and pinite. Dashes indicate analyses below the detection limit. Complete results are shown in the electronic supplementary material 2.2

Oxide (wt%)	Detection Limits	PT03		K5533		K5538	
		Crd	Pin	Crd	Pin	Crd	Pin
SiO_2	0.002	48.90	43.51	49.03	40.75	40.59	40.6
Al_2O_3	0.016	33.21	36.48	34.14	34.23	29.14	37.63
FeO	0.05	7.81	1.87	8.46	5.01	10.46	2.95
MnO	0.07	0.39	-	0.28	-	0.05	-
MgO	0.016	8.16	0.12	8.30	3.81	3.81	0.38
CaO	0.006	0.03	0.19		0.25	4.47	1.1
Na_2O	0.024	0.39	0.26	0.28	0.20	0.4	0.38
K_2O	0.024	-	0.38	-	2.17	0.07	-
Total		98.88	82.81	100.50	86.50	89	83.17
Apfu		18 O	14 O	18 O	14 O	18 O	14 O
Si		5.00	3.94	4.95	3.71	4.8	3.70
Al		4.00	3.89	4.06	3.67	4.1	4.04
Fe		0.67	0.13	0.71	0.36	1	0.21
Mn		0.03	0.00	0.02	0.01	-	0.00
Mg		1.24	0.01	1.25	0.29	0.7	0.03
Ca		0.00	0.03	0.00	0.03	0.6	0.15
Na		0.08	0.03	0.05	0.02	0.1	0.04
K		0.00	0.07	0.00	0.38	-	0.02
Oxide (wt%)	Detection Limits	L44		L14G		L10A	
		Crd	Pin	Crd	Pin	Crd	Pin
SiO_2	0.002	49.54	43.06	49.39	43.96	46.99	44.13
Al_2O_3	0.016	34.29	34.19	34.16	38.96	32.26	36.33
FeO	0.05	5.96	6.04	8.05	1.46	8.79	0.84
MnO	0.07	-	-	-	-	0.32	-
MgO	0.016	10.00	3.22	8.67	0.31	7.32	-
CaO	0.006	-	0.36	0.02	0.36	-	0.48
Na_2O	0.024	-	0.13	0.09	0.10	0.24	0.15
K_2O	0.024	-	1.85	-	0.32	-	0.32
Total		99.81	88.83	100.37	85.49	95.90	82.25
Apfu		18 O	14 O	18 O	14 O	18 O	14 O
Si		4.96	3.79	4.97	3.85	4.97	3.99
Al		4.05	3.55	4.05	4.02	4.07	3.87
Fe		0.50	0.42	0.68	0.10	0.78	0.06
Mn		0.00	0.00	0.00	0.00	0.03	0.00
Mg		1.49	0.24	1.30	0.02	1.16	0.00
Ca		0.00	0.05	0.00	0.05	0.00	0.07
Na		0.00	0.01	0.02	0.01	0.00	0.02
K		0.00	0.32	0.00	0.05	0.00	0.05

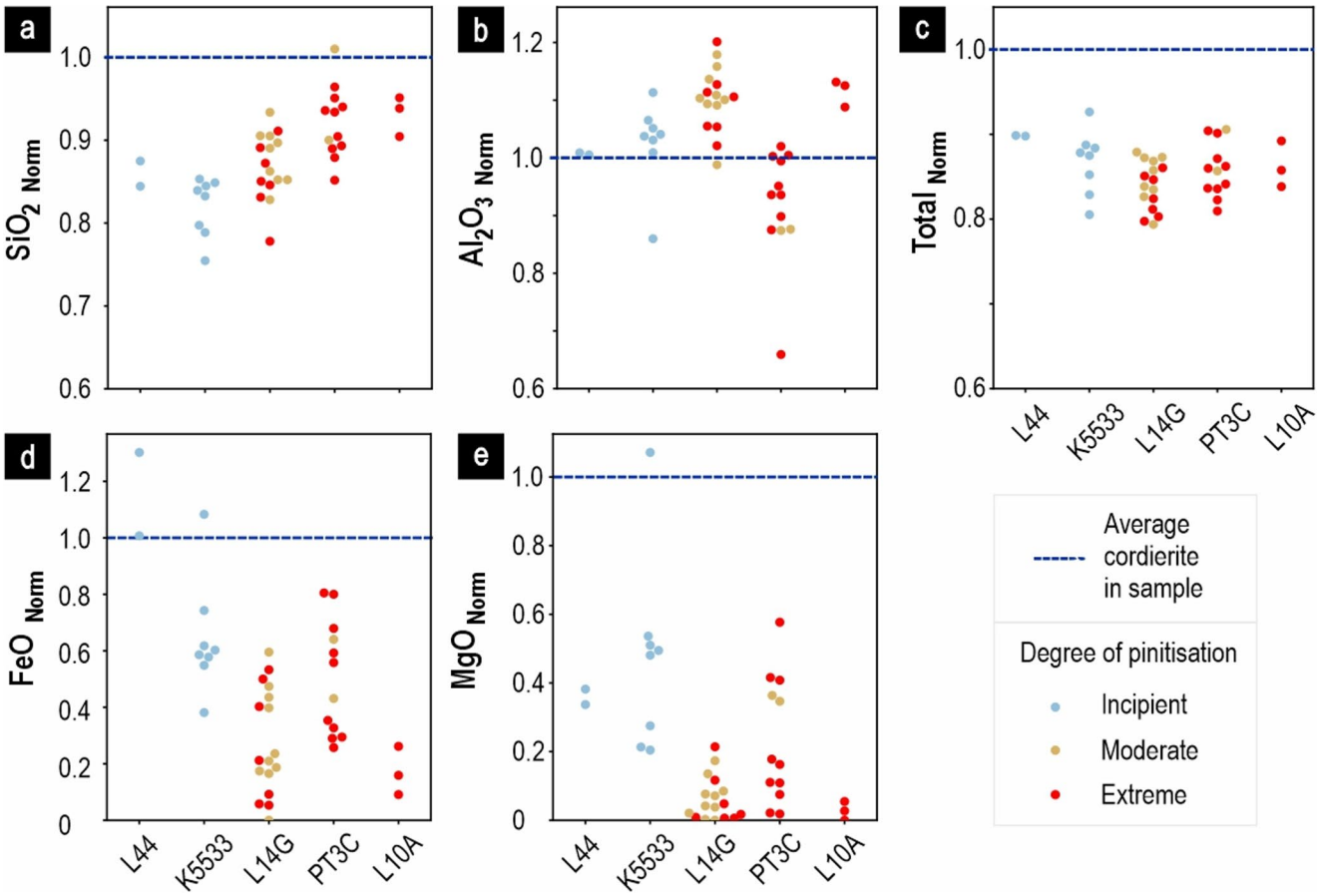

Fig. 3 Swarm plot showing the **a** SiO_2, **b** Al_2O_3, **c** Totals, **d** FeO, and **e** MgO composition of pinite in different samples normalised to the average cordierite composition in each sample. Marker colours correspond to the degree of pinitization. A swarm plot is used here to avoid overlap between data points

Trace element concentrations

Biotite (sample PT22A) is the main host of Li, V, Rb and Cs, a secondary host of Sc, Cr, Co, Ni, Zn, Nb and Sn, and a less prominent host of Ta and W (Fig. 4). Chlorite hosts similar concentrations of Li (Fig. 4a), Co, Ni and Zn to biotite (~250 ppm), and muscovite and chlorite host V and Cr in similar concentrations to biotite (~240–270 ppm). In comparison with biotite, muscovite hosts more Sn and Sc (~18.6 ppm Sn and ~65.1 ppm Sc in comparison with ~11.8 ppm and ~18.6 ppm – Fig. 4b), and ilmenite and rutile host more Nb, Ta and W (biotite contains ~63 ppm Nb, ~4.43 ppm Ta and ~3.77 ppm W, while titanium oxides contain ~940–1868 ppm Ta, ~58.7–131 ppm Ta and ~49–189 ppm W – Figs. 4d–f). Other analysed phases host considerably less Cs than biotite, which contains ~38.5 ppm Cs (Fig. 4c).

The concentrations of Li, Be and Cs hosted in cordierite vary between samples. Compared with the average concentration of cordierite in each sample, Li concentrations in pinite vary with the degree of pinitization: in samples where cordierite is incipiently pinitized, pinite has up to one order of magnitude more Li (e.g., cordierite contains ~14.5 ppm Li and pinite contains 375–523 ppm Li in the most pristine sample – L44), while in samples where cordierite is extremely pinitized, pinite has up to one order of magnitude less Li (e.g., cordierite and pinite contain 419 and 73 ppm Li, respectively, in sample L10A – Fig. 5a). Pinite Be concentrations in incipiently pinitized samples are nearly up to 1.5 times higher than the sample average cordierite (e.g., pinite contains ~25.5 ppm Be and cordierite 19.7 ppm in sample K5533), while Be concentrations in pinite in samples with extreme pinitization are around ~73 ppm, while cordierite in that sample (L10A) contains 419 ppm Be. Samples with variable degrees of pinitization (PT03 and L14G) show contrasting behaviour (Fig. 5b). Pinite Cs concentrations in incipiently pinitized samples are up to 6 times higher (pinite contains 12–27 ppm Cs and cordierite contain ~4.38 ppm Cs in sample L44), while pinites in samples with moderate to nearly complete pinitization have significantly lower Cs concentrations (e.g., sample L14G cordierites contain ~4.08 ppm Cs and pinites contain 0.53 ppm).

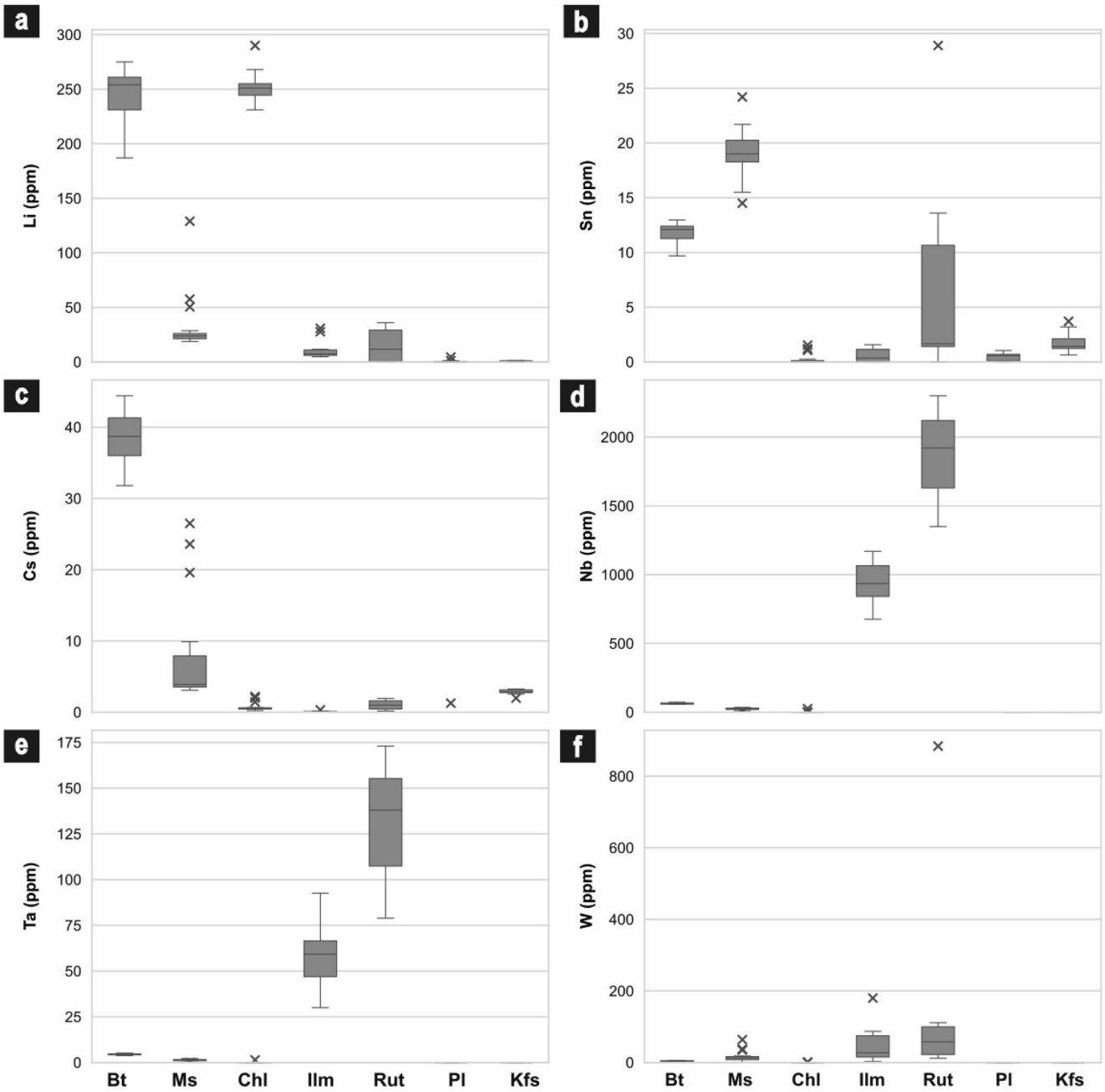

Fig. 4 Box plots illustrating the range of concentrations of **a** Li, **b** Sn, **c** Cs, **d** Nb, **e** Ta, and **f** W in key phases in sample PT22A. The central line in each box represents the median concentration, while the top and bottom edges of the box represent the first (Q1) and third (Q3) quartiles, respectively. The vertical lines ('whiskers') extend to the minimum and maximum values within 1.5 times the interquartile range (IQR) from the quartiles. Data points outside this range (outliers) are plotted individually

Other elements are present in significantly higher concentrations in pinite than cordierite in samples L14G or PT03C (Fig. 6). For instance, pinite in PT03C contains up to 300 times more Ni (~306 ppm), 90 times more Cu (~196 ppm) and 130 times more P (~1287 ppm) than the average cordierite in the sample, which contains ~4.5 ppm Ni, ~6.9 ppm Cu, and 40 ppm P (Figs. 6a–c). Moreover, pinite in samples K5533 contains up to 110 times more Y (~17.1 ppm Y in pinite versus ~0.27 ppm in cordierite) and L14G pinite has up to 60 times more V and Rb (~10 and 12.5 ppm) than the average sample cordierite (~0.07 and ~0.54 ppm). No variations in trace element concentration were observed between core and rim of minerals in all samples.

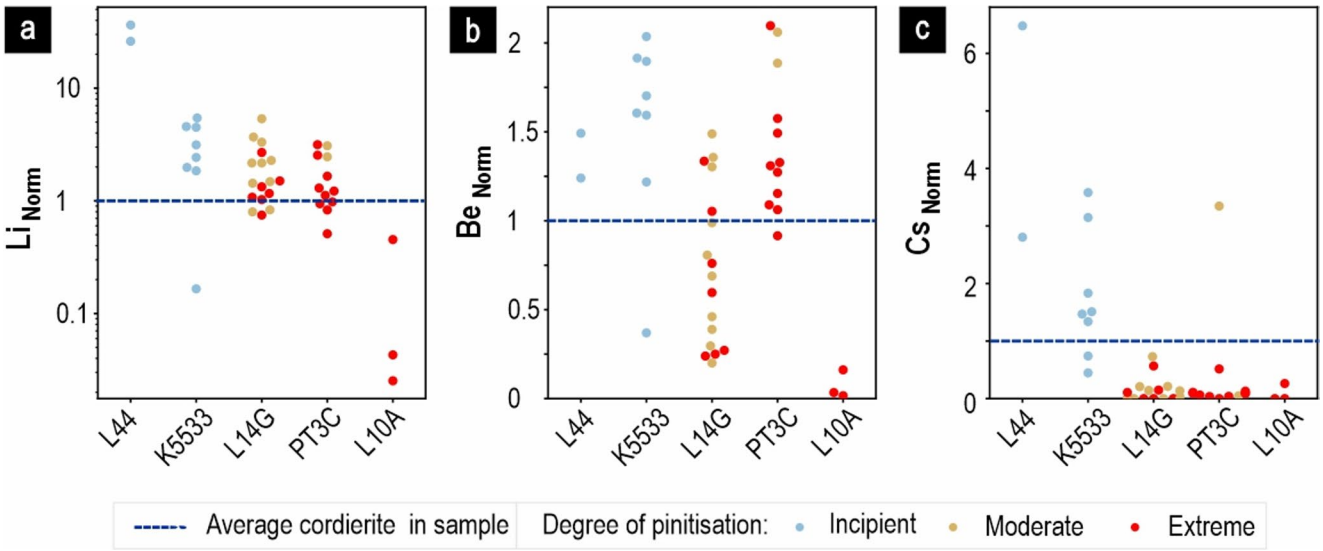

Fig. 5 Swarm plot showing the concentration **a** Li, **b** Be, and **c** Cs in pinites in different samples, normalised to the average composition of cordierites in each sample. Marker colours correspond to the degree of pinitization. A swarm plot is used here to avoid overlap between data points

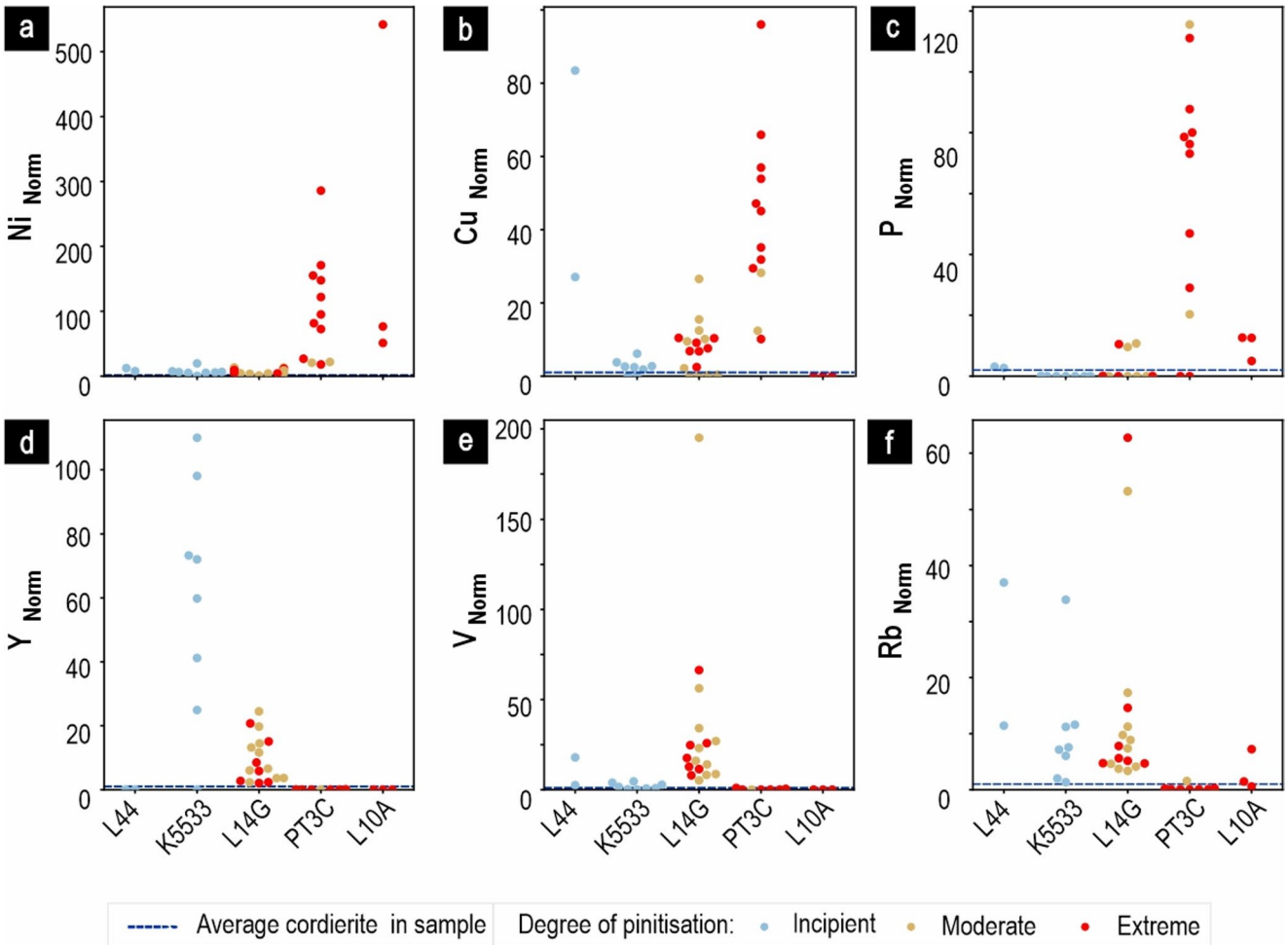

Fig. 6 Swarm plot showing the concentration **a** Ni, **b** Cu, **c** P, **d** Y, **e** V, and **f** Rb in pinites in different samples normalised to the average composition of cordierites in each sample. Marker colours correspond to the degree of pinitization. A swarm plot is used here to avoid overlap between data points

Table 5 Bulk-rock composition and calculated fresh and altered domain compositions in sample PT22A

		PT22A			
	Oxide (wt%)	Limit of Detection	Bulk-rock		Calculated
		Analysed	Normalised	Fresh	Altered
SiO_2	0.01	65.46	68.4	69.8	68.7
TiO_2	0.001	0.752	0.8	0.4	0.3
Al_2O_3	0.01	15.21	15.9	16.1	16.3
FeO_{Total}	0.01	5.6	5.7	2.7	3.8
MnO	0.001	0.064	0.1	0	0
MgO	0.01	1.78	1.9	1.1	1.5
CaO	0.01	1.47	1.5	2.1	1.5
Na_2O	0.01	2.31	2.4	3.5	2.6
K_2O	0.01	3.6	3.8	3.6	3.6
P_2O_5	0.01	0.14			
LOI	0.01	2.03			
H_2O	0.01			0.7	1.7
Total		98.42	100	100	100

Bulk-rock and domain compositions of sample PT22A

The calculated altered and fresh domain compositions in sample PT22A were typically within 0.5–1.5 wt% of the bulk-rock composition (normalised to 100%) except for FeO (Table 5; Fig. 7; Electronic Supplementary Materials 2.4 and 2.5). The fresh domain has more SiO2, CaO and Na2O, and less FeO and H2O than the altered domain, which is more similar to the measured composition (Fig. 7).

Temperature and fluid content estimates of sample PT22A

Temperature estimates for sample PT22A show different temperature conditions for the fresh and altered domains, which was expected since their petrographies are related to peak metamorphism and retrogression conditions,

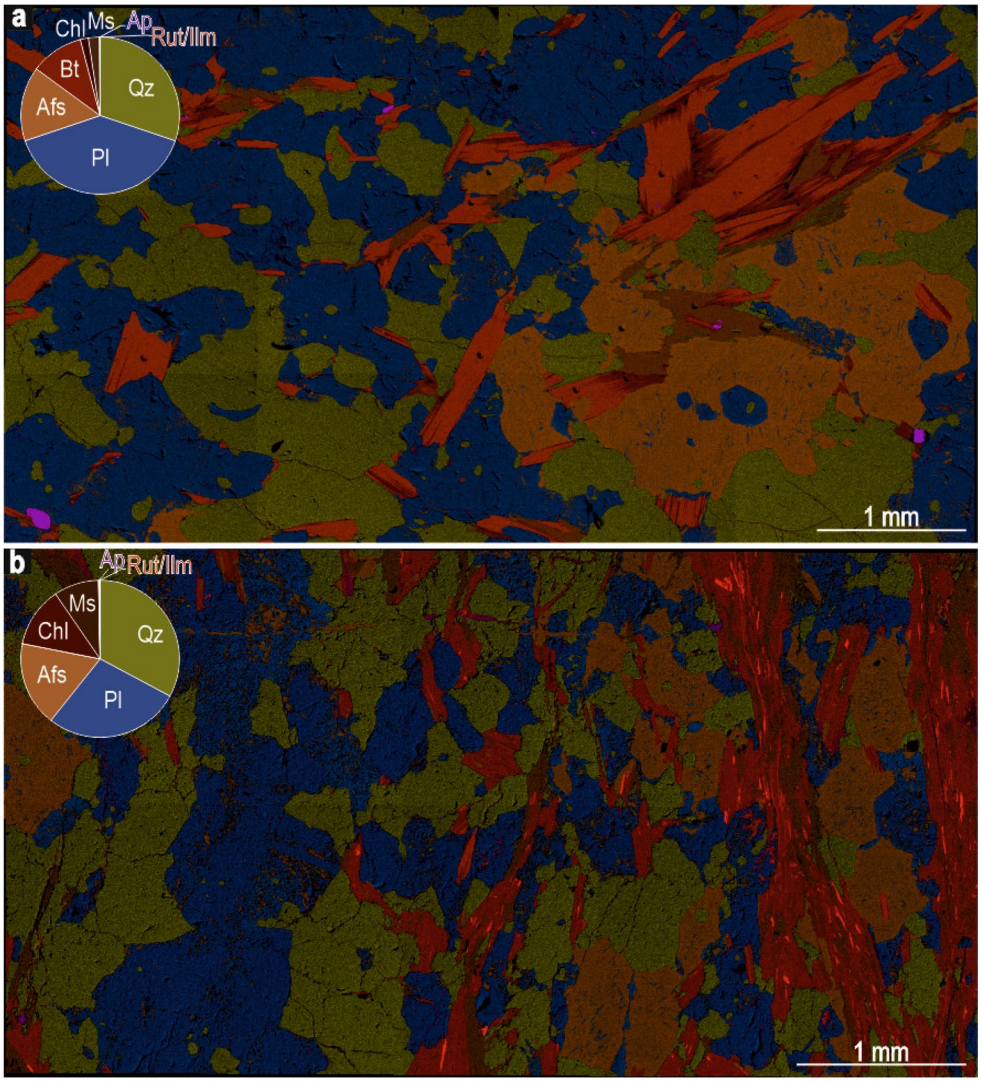

Fig. 7 EDS-SEM compositional maps of domains of sample PT22A with colours based on selected oxides. **a** Fresh domain composed mainly of biotite, quartz and feldspars, some chlorite, muscovite, rutile and ilmenite, and accessory apatite. **b** The altered domain is composed mainly of chlorite, muscovite, quartz, less feldspar, less rutile and ilmenite, and accessory apatite

respectively. Single crystal temperature estimates for fresh domains are 630–690 °C (Ti-in-biotite), while altered domains record temperatures between 340 and 540 °C (Zr-in-rutile) and 280–440 °C (2 kbar) or 360–540 °C (8 kbar - chlorite thermometer – Fig. 8). Similarly, phase equilibria modelling also highlights that the biotite in the fresh domain records higher temperatures (>750 °C) and is not in equilibrium with either chlorite or muscovite (Fig. 9a); while modelling of the altered domain (Fig. 9b) indicates conditions of around 350–500 °C (based on the stability field of 0.1 to 2.2 vol% chlorite). Although the altered domain shows fields with the stability of all mineral products formed by the chloritization of biotite (chlorite, muscovite, ilmenite, and rutile), the volumes of chlorite and muscovite vary significantly from those observed in the compositional maps (Fig. 9b). While modelling results show about 0.1 to 2.2 vol% of chlorite and muscovite volumes up to 22%, the compositional map of the altered domain shows about 12% of chlorite and 9% of muscovite. In the model, the higher volumes of muscovite are likely linked to the absence of alkali-feldspars, while the higher volumes of chlorite are likely linked to higher fluid input, as shown below.

A T-X diagram with H_2O varying between 0.6 and 3 wt% was used to verify the amount of fluid necessary to drive the complete breakdown of biotite. Chlorite volumes reach 11 vol% with water contents between 2.4 and 3 wt% (Fig. 10a), which is similar to the volume estimated from thin section. Biotite volumes are higher between 1.2 and 1.8 wt% water and decrease with increasing water content and chlorite volumes (Fig. 10b). Muscovite volume increases with increasing water contents, up to 30% (Fig. 10c), which is much higher than observed in the thin section. In the model, the higher muscovite volumes are due to the complete breakdown of alkali-feldspar, which is not observed in thin section. In fields with high water contents, rutile and ilmenite are not stable, and low volumes of epidote are predicted (<3%). The T-X diagram corroborates that higher water contents are necessary for the complete breakdown of biotite, but the model fails to perfectly reproduce the petrographic observations.

Mass transfer of sample PT22A

Mass transfer estimates during the biotite-chlorite transition are illustrated in Fig. 11 (full results on Electronic Supplementary Materials 2.6 and 2.7). The results indicate that concentrations of Cr, Ni and W remain constant (i.e. the difference in average values lying between ±20%), while Cs (99 to 67% loss) and Tl (97 to 57% loss) are nearly completely lost. Moderate loss of Li (32 to 56%), Zn (26 to 50%), and Sn (30 to 82%) is expected in the minimum to maximum stoichiometric and visual estimates. Results for Sc, V, Co, Nb and Ta are inconclusive since average and minimum results vary for each estimate.

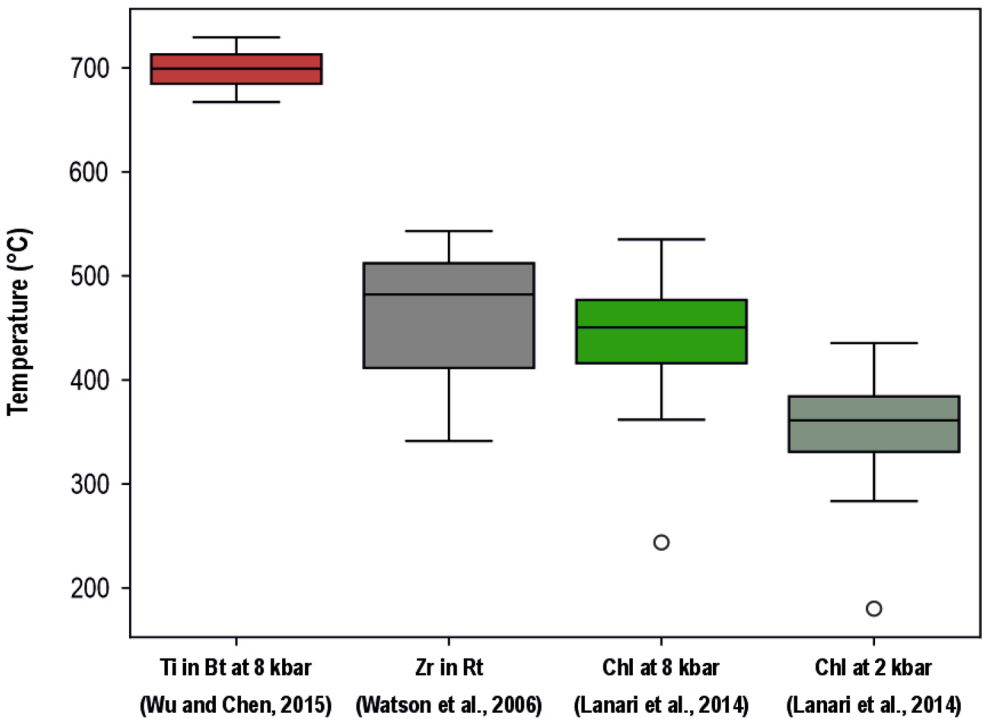

Fig. 8 Box plot illustrating the geothermometer estimates for sample PT22A. The central line in each box represents the median concentration, while the top and bottom edges of the box represent the first (Q1) and third (Q3) quartiles, respectively. The vertical lines ('whiskers') extend to the minimum and maximum values within 1.5 times the interquartile range (IQR) from the quartiles. Data points outside this range (outliers) are plotted individually

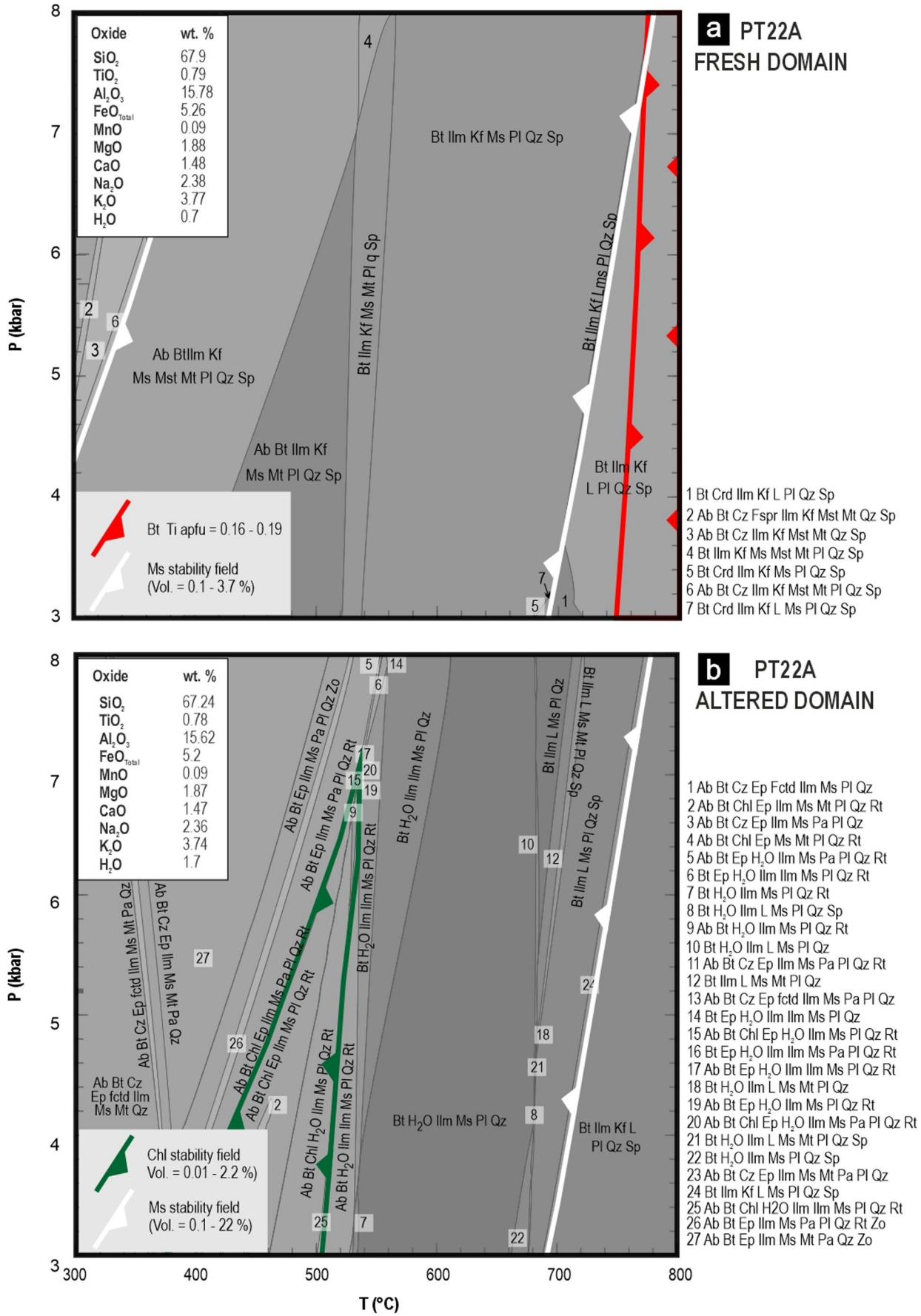
a PT22A
FRESH DOMAIN
Oxide wt. %
SiO2 67.9
TiO2 0.79
Al2O3 15.78
FeOTotal 5.26
MnO 0.09
MgO 1.88
CaO 1.48
Na2O 2.38
K2O 3.77
H2O 0.7
Bt Ti apfu = 0.16 - 0.19
Ms stability field
(Vol. = 0.1 - 3.7 %)
Ab BtIlm Kf
Ms Mst Mt Pl Qz Sp
Ab Bt Ilm Kf
Ms Mt Pl Qz Sp
Bt Ilm Kf Ms Mt Pl q Sp
Bt Ilm Kf Ms Pl Qz Sp
Bt Ilm Kf Lms Pl Qz Sp
Bt Ilm Kf
L Pl Qz Sp
1 Bt Crd Ilm Kf L Pl Qz Sp
2 Ab Bt Cz Fspr Ilm Kf Mst Mt Qz Sp
3 Ab Bt Cz Ilm Kf Mst Mt Qz Sp
4 Bt Ilm Kf Ms Mst Mt Pl Qz Sp
5 Bt Crd Ilm Kf Ms Pl Qz Sp
6 Ab Bt Cz Ilm Kf Mst Mt Pl Qz Sp
7 Bt Crd Ilm Kf L Ms Pl Qz Sp
b PT22A
ALTERED DOMAIN
Oxide wt. %
SiO2 67.24
TiO2 0.78
Al2O3 15.62
FeOTotal 5.2
MnO 0.09
MgO 1.87
CaO 1.47
Na2O 2.36
K2O 3.74
H2O 1.7
Chl stability field
Vol. = 0.01 - 2.2 %)
Ms stability field
(Vol. = 0.1 - 22 %)
Ab Bt Cz
Ep fctd Ilm
Ms Mt Qz
Ab Bt Cz Ep fctd Ilm Ms Mt Pa Qz
Ab Bt Cz Ep Ilm Ms Mt Pa Qz
Ab Bt Ep Ilm Ms Pa Pl Qz Zo
Ab Bt Ep Ilm Ms Pa Pl Qz Rt
Ab Bt Chl Ep Ilm Ms Pa Pl Qz Rt
Ab Bt Chl Ep Ilm Ms Pl Qz Rt
Ab Bt Chl H2O Ilm Ms Pl Qz Rt
Ab Bt H2O Ilm Ms Pl Qz Rt
Bt H2O Ilm Ms Pl Qz
Bt H2O Ilm Ms Pl Qz
Bt Ilm L Ms Pl Qz
Bt Ilm L Ms Mt Pl Qz Sp
Bt Ilm L Ms Pl Qz Sp
Bt Ilm Kf L
Pl Qz Sp
1 Ab Bt Cz Ep Fctd Ilm Ms Pl Qz
2 Ab Bt Chl Ep Ilm Ms Mt Pl Qz Rt
3 Ab Bt Cz Ep Ilm Ms Pa Pl Qz
4 Ab Bt Chl Ep Ms Mt Pl Qz Rt
5 Ab Bt Ep H2O Ilm Ms Pa Pl Qz Rt
6 Bt Ep H2O Ilm Ilm Ms Pl Qz Rt
7 Bt H2O Ilm Ms Pl Qz Rt
8 Bt H2O Ilm L Ms Pl Qz Sp
9 Ab Bt H2O Ilm Ms Pl Qz Rt
10 Bt H2O Ilm L Ms Pl Qz
11 Ab Bt Cz Ep Ilm Ms Pa Pl Qz Rt
12 Bt Ilm L Ms Mt Pl Qz
13 Ab Bt Cz Ep fctd Ilm Ms Pa Pl Qz
14 Bt Ep H2O Ilm Ilm Ms Pl Qz
15 Ab Bt Chl Ep H2O Ilm Ms Pl Qz Rt
16 Bt Ep H2O Ilm Ilm Ms Pa Pl Qz Rt
17 Ab Bt Ep H2O Ilm Ilm Ms Pl Qz Rt
18 Bt H2O Ilm L Ms Mt Pl Qz
19 Ab Bt Ep H2O Ilm Ms Pl Qz Rt
20 Ab Bt Chl Ep H2O Ilm Ms Pa Pl Qz Rt
21 Bt H2O Ilm L Ms Mt Pl Qz Sp
22 Bt H2O Ilm Ms Pl Qz Sp
23 Ab Bt Cz Ep Ilm Ms Mt Pa Pl Qz
24 Bt Ilm Kf L Ms Pl Qz Sp
25 Ab Bt Chl H2O Ilm Ilm Ms Pl Qz Rt
26 Ab Bt Ep Ilm Ms Pa Pl Qz Rt Zo
27 Ab Bt Ep Ilm Ms Mt Pa Qz Zo
P (kbar)
T (°C)

Fig. 9 Simplified pseudosections of sample PT22A at 3 to 8 kbar and 300 to 800 °C based on the amount of water in the **a** fresh and **b** altered domain added to the normalised bulk-rock composition

Discussion

The results of this study provide potential mechanisms for how the biotite to chlorite and cordierite to pinite retrograde reactions can release different trace elements.

As biotite reacts to form chlorite, elements mobilise according to how well the product minerals can act as hosts (Fig. 11). For example, Cs is nearly completely mobilised since no products of the reaction host Cs as effectively as biotite. By contrast, reaction products can only host some of the Sn and Li released from biotite, causing moderate mobilisation of these two elements. Tungsten, Nb and Ta are not mobilised, since their main mineral hosts (muscovite, ilmenite, and rutile) are mineral products of the reaction (possible for rutile and ilmenite). The reaction of biotite to chlorite may also remove major elements such as K from the system through the fluid, which can potentially lead to chlorite formation without forming much or any muscovite, which, in turn, would allow for Sn and W to be more readily removed from the system.

The retrograde breakdown of biotite at different conditions (temperature, but also pressure) will produce different mineral products and/or stoichiometry, affecting the mobilisation of different trace elements (e.g. Yang et al. 2023). In the studied sample, chlorite and rutile are both products of the reaction and record temperatures around 350–500 °C (Figs. 10 and 11). However, under different conditions, different mineral products could be formed during the reactions, leading to different trace elements being mobilised or sequestered, e.g., as shown for Nb by Yang et al. (2023). These authors show that specific biotite retrograde reactions occurring at different P-T conditions enhance/hinder the mobilisation of Nb and the formation of Nb-rich phases. This observation and the variety of retrograde reactions highlight the need for more studies focusing on trace element transfer during retrograde reactions.

Lithium, Be, and Cs all mobilise during cordierite breakdown, but to varying degrees depending on the degree of pinitization (Fig. 5). The trends in Li and Cs concentrations suggest increased mobilisation with increasing pinitization, while Be shows both enrichment and depletion in moderately pinitized samples. Samples PT03 and L14G show no clear geochemical differences in composition between moderately and extremely pinitized cordierites (Figs. 4, 6 and 7), suggesting that their varied appearance may be an artefact of 2D cuts of the thin section or that different parameters affect the mobilisation of Li, Be and Cs. The full controls are still somewhat unclear. Any links between the type of pinite and their effect on mass transfer are still unclear, as the samples analysed in this investigation produced only mat- and i-type pinites. Further studies are necessary to understand the effect of pinite type on the fate of trace elements hosted by cordierite.

Concentrations of Li, Cs and Be correlate with major elements, especially Fe and Mg, in pinite (Fig. 12), suggesting that their mobilisation depends on the clay minerals formed during pinitization. The SiO2, Al2O3 and volatile concentrations in the pinites match clays in the kaolinite group. However, FeO and MgO vary from nearly negligible amounts up to the same percentages as cordierite. Such variations suggest that either the fine-grained pinite aggregates are a mixture of clays from the kaolinite and smectite groups or that the analysis is a mixture of pinite and cordierite. The former is more likely because the analysis totals indicate a volatile content similar to clay minerals rather than intermediate compositions between cordierite and clay minerals. This agrees with previous studies that suggested smectite group clays are key hosts of Li (e.g., Zhao et al. 2023 and references therein). Therefore, the mobilisation of Li, Be, and Cs during pinitization is enhanced when pinite fine-grained aggregates are composed of clays with lower FeO and MgO than smectite.

The role of fluid flux and composition

High volumes of percolating fluid are necessary to mobilise trace elements during retrogression reactions because fluids are needed both to drive the reaction itself and to transport these elements out of the system. In the case of chloritization, our calculation showed that a water content of around 2.5 wt% is necessary to alter biotite completely in our studied sample (Fig. 10). As the current volatile content of the samples is 1.7 wt% (altered domain) it can be assumed that around 1 wt% of fluid left the system, potentially enriched in Cs, Sn and Li. In the case of pinitization, our results show that the percolation of fluids enhances the mobilisation of Li and Be because it can potentially also remove Fe and Mg, which will favour the genesis of pinite with lower Li and Be concentrations (kaolinite). Hence, high fluid volumes and mobility are essential both to trigger pervasive retrograde alteration and to carry the trace elements released during retrograde reactions out of the system.

Mobilisation of trace elements during the retrograde breakdown of biotite also clearly depends on fluid compositions. Although we have no data on the composition of the fluid, previous studies have shown, for example, that acidic environments enhance biotite alteration (Eggleton and Banfield 1985; Li et al. 2014); that Sn is more readily mobilised by Cl-bearing reduced fluids with low pH (Liu et al. 2023); and that W is more readily mobilised in F-bearing, acidic to neutral (pH < 8) fluids (Mei et al. 2025). Fluid compositions

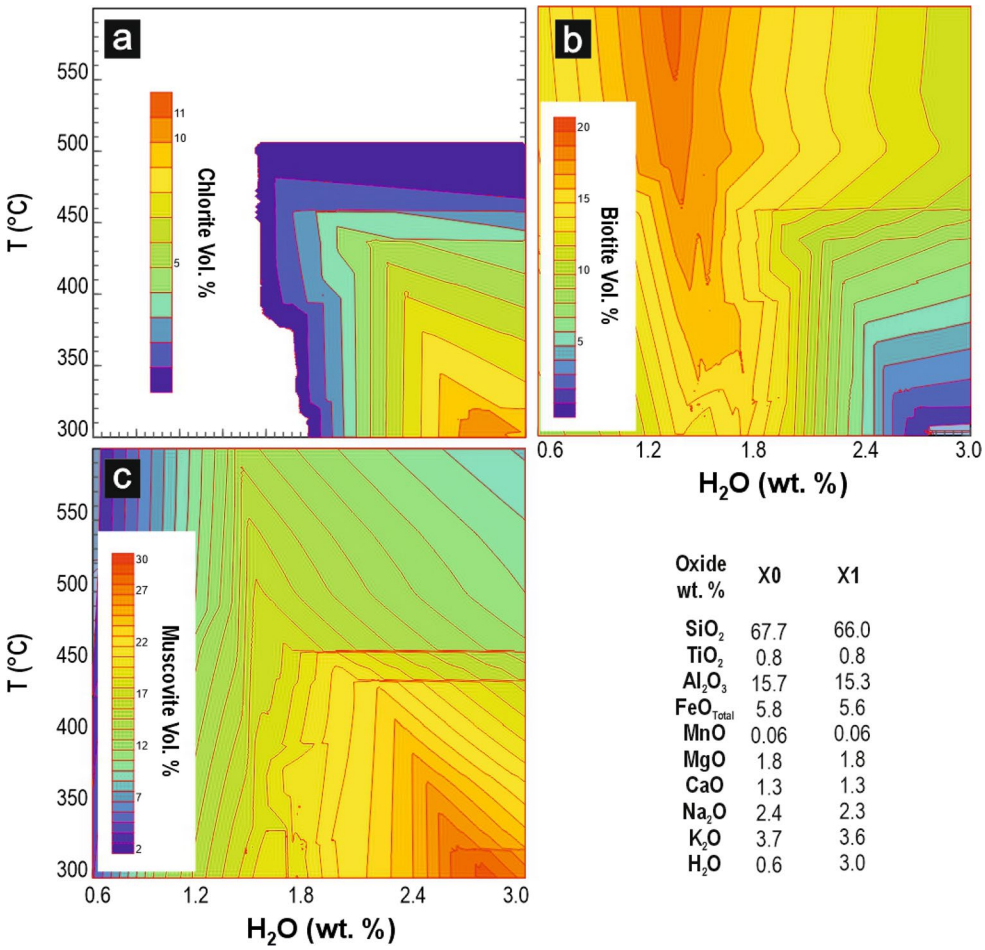

Fig. 10 T-X diagrams (at 3 kbar) showing the vol% variations of **a** chlorite, **b** biotite and **c** muscovite between 300 to 600 °C and 0.6 to 3 wt% water

can furthermore change over time or with different fluid pulses. For instance, cooling can oxidise fluids, while the greisenization of the host rocks can cause pH neutralisation, which makes fluid transport of Sn less efficient (Liu et al. 2023) and can probably explain differences between chlorite and muscovite trace element budgets near the source and along pathways of fluids (as is likely the case for sample PT22A) versus near deposits (e.g., Chen et al. 2023; Monnier et al. 2022).

The composition of the fluid also seems to be one of the key controls on the mobility of the trace elements during pinitization. Contrary to our findings, kaolinite has previously been suggested as a key host of Li in mudstones (Zhang et al. 2022). These divergent findings suggest that the partitioning of Li between kaolinite and fluids can favour one phase or the other depending on fluid composition and pH: Hoyer et al. (2015) show that kaolinite's capability to adsorb Li varies greatly with pH. Similarly, abnormal concentrations of Ni, Cu, P, Y, V and Rb in pinite in samples PT3C and L14G (Fig. 6) could be evidence for the influx of fluids with different compositions in each geological setting. This would suggest that contrasting Be concentrations in pinite in samples PT3C and L14G (Fig. 6) could also be explained by Be partitioning depending on fluid composition. Enhanced Be mobilisation in soils has previously been associated with low-pH conditions (Åström et al. 2018; and references therein).

Fluid sources

The geological setting of the samples – migmatites formed in the late stages of Variscan orogen, which is marked by partial melting and voluminous granitic intrusions (~295–330 Ma – e.g., Finger et al. 1997; Finger and Clemens 1995) – hints that dehydration reactions during prograde metamorphism and/or from the crystallisation of magmas are the most likely sources of fluids that triggered retrogression. For instance, sample PT22A comes from the Tormes Gneissic Dome lower unit (Portugal/Spain border), which is composed of high-grade ortho and paragneisses intruded by syn- and late-Variscan granitoids (~320 Ma – López-Moro et al. 2012; Viruete et al. 2000; details in the Supplementary Text). While previous studies of fluid inclusions in quartz veins from the Central Iberian Massif documented magmatic-hydrothermal fluid signatures (e.g., Caldevilla et al. 2023; Neiva 2008),

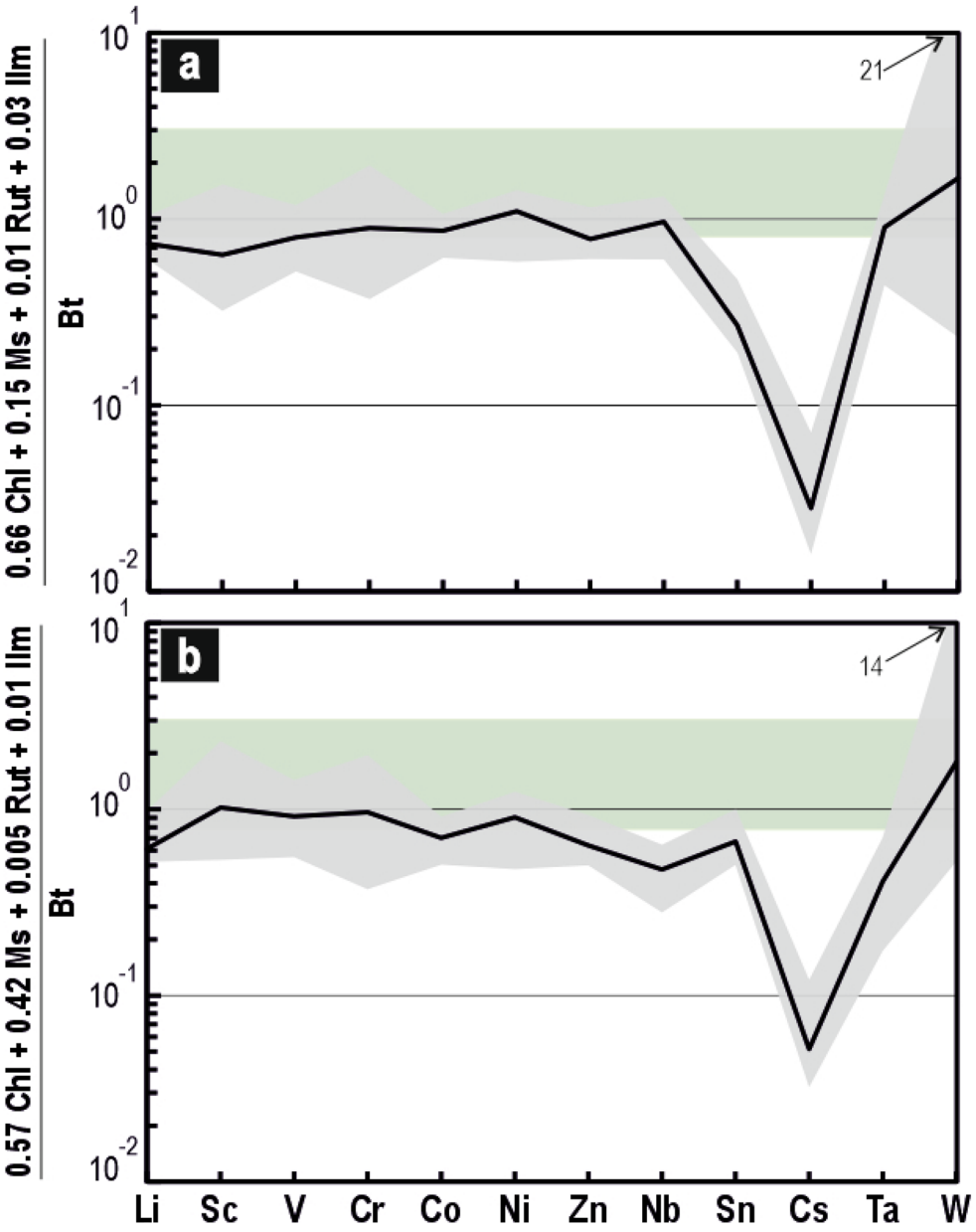

Fig. 11 **a** Stoichiometric and **b** visual estimates of mass transfer for the chloritization of biotite. Grey shaded area indicates the ranges of mass transfer based on maximum and minimum trace element concentrations, and the black line indicates an estimate based on average trace element concentrations in the reaction minerals. The green shaded area indicates a ± 20% difference in mass in relation to biotite (y = 1). The y-axis of the stoichiometric estimate is based on the molar stoichiometry of the reactions converted to product weight, normalized to biotite weight. Numbers indicated by arrows (21 and 14) indicate W maximum estimates

metamorphic fluid signatures have also been observed in fluid inclusions across the Central Iberian Zone (e.g.,Antona et al. 1994; Cathelineau et al. 2020; Noronha 2017; Noronha et al. 1992), including 25 km to the SSW of sample PT22A (Antona et al. 1994). Hence, the chloritization of biotite in the sample PT22A was likely either triggered by fluid released from nearby magma crystallisation or by the circulation of metamorphic fluids, or a mixture of both.

Similarly, the geological setting of the pinitized cordierite-bearing samples hints at possible sources of fluids (details in the Supplementary Text). Shear zones have been documented across the Agly massif (Aumar et al. 2022; Tartèse et al. 2012) and are known to act as channels for fluid; thus, channelised fluid flow may help explain why extremely sheared samples from the area (L14G and L10A) show a higher degree of pinitization and trace element mobility than the undeformed and incipiently pinitised sample L44. In the Mindelo Complex, fluids released from the crystallisation of nearby magmas (Silva 2014) may have caused the pinitization in the un-deformed sample PT03C. Nevertheless, meteoric water is also a potential source of fluid since the formation of clays occurs at temperatures (< 200 °C). Further geochemical or isotopic data is required to constrain the nature of the fluid sources in each of those cases.

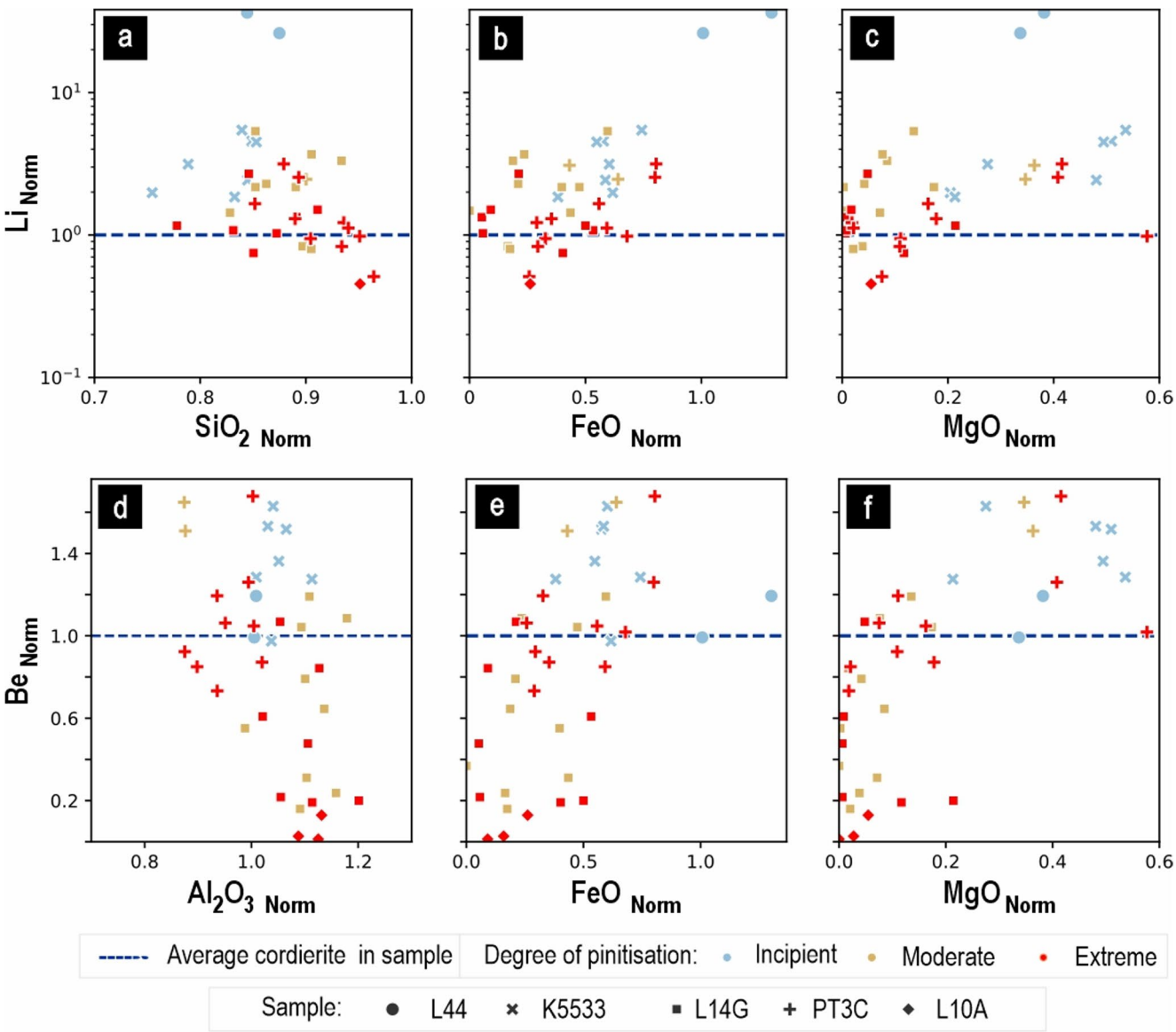

Fig. 12 Distribution of Li against **a** SiO_2, **b** FeO, and **c** MgO in pinites; and Be against **d** Al_2O_3, **e** FeO, and **f** MgO in pinite normalised to the average concentrations of cordierite in each sample

Implications

This study shows that fluid-induced breakdown of biotite and cordierite mobilises trace elements, which are transported out of the system by fluids. These reactions, therefore, have the potential to generate fluids enriched in specific critical elements (specifically Li, Be and Cs from the pinitization of cordierite, and Li, Sn and W from the chloritization of biotite), which, in turn, could be a factor in the production of unconventional deposits such as veins, hydrothermal alterations, brines, and clays. While the potential connection between our results and such deposits is briefly discussed below, it is important to note that these retrogression reactions will not always produce deposits since this depends on many other factors, including the volumes of fluid and host minerals, the migration capacity of the fluid, and the occurrence of optimal fluid compositions for the uptake of ore-forming elements in the fluid.

Magmatic fluids are typically the main contributor (Yuan et al. 2018) to Sn- and W-rich fluids. However, in some hydrothermal deposits, the retrograde alteration of biotite has been suggested to generate/enhance high concentrations of fluid-borne Sn (Xie et al. 2010) and/or Nb-Ta mineralisation (Yang et al. 2020, 2023), and basement rocks (paragneiss and granite) have been shown as potential exclusive sources of ore fluids (Walter et al. 2019). For instance, the chloritization of biotite from basement rocks might produce

enriched fluids that contribute to the widespread Sn and (potentially) W quartz-vein deposits across the Central Iberian Zone (e.g., Sinclair et al. 2011) since fluid inclusion studies in the nearest deposits to sample PT22A show metamorphic fluid signatures (Antona et al. 1994–25 km to the SSW). Similarly, the breakdown of cordierite may play a role in the origin of Li-rich clays in sedimentary deposits or the source of Li-rich geothermal fluids, since the pinitization of cordierite is often observed in samples where micas – commonly suggested as sources of Li – are still fresh (e.g., Sanjuan et al. 2022). Moreover, the remobilisation of Be due to the pinitization of cordierite might contribute to the genesis of non-conventional occurrences of hydrothermal/metamorphic Li-Mg-Fe-rich beryl hosted in calcite-quartz veins crosscutting low-grade metamorphic rocks (Novák et al. 2011).

Conclusions

This study highlights that the breakdown of biotite and cordierite can extensively remobilise critical elements and potentially release them into retrograde lower-temperature fluids. The breakdown of biotite to chlorite, muscovite, ilmenite and rutile around 350–500 °C mobilises Li, Cs, and Sn. Reactions that break down biotite without producing muscovite may also mobilise W, since muscovite stores most W released from biotite. Similarly, the breakdown of cordierite below ~200 °C to pinite composed of clay minerals with low FeO and MgO contents favours the release of Li and Be into the fluid. Moreover, our findings indicate the mobilisation of trace elements during both reactions is linked to high volumes of fluid percolation to enhance pervasive alteration and remove major components (such as FeO and MgO) and specific fluid compositions that enhance trace element partitioning (Åström et al. 2018; Eggleton and Banfield 1985; Hoyer et al. 2015; Li et al. 2014; Liu et al. 2023; Mei et al. 2025).

Further research about how specific retrograde reactions mobilise trace elements and contribute to enriched fluid genesis is necessary since different fluid compositions, as well as pressure and temperature conditions, will change reaction stoichiometries and element partitioning. Moreover, the link between specific retrograde reactions, enriched fluids, and the genesis of less conventional deposits such as clay-type deposits, geothermal brines, and mineralised quartz veins still depends on precise volumetric constraints to determine if retrograde reactions can wholly account for the high concentrations observed in such deposits.

Supplementary Information The online version contains supplementary material available at https://doi.org/10.1007/s00710-026-00972-2.

Acknowledgements We acknowledge funding from the European Union's Horizon 2020 research and innovation programme under the Marie Skłodowska-Curie [grant agreement No. 956125] for E.O.C.'s PhD as part of the Innovative Training Network "FluidNET". We would also like to thank Michelle Higgins and Kay Knight for help with sample preparation at The Open University. Giulia Degli-Alessandrini with the scanning electron microscope and electron probe microanalysis at The Open Univeristy and Eric Hellebrand for all his help with electron probe microanalysis at the University of Utrecht.

Author contributions Elisa Oliveira da Costa: Conceptualization, Methodology, Investigation, Formal Analyses, Data Curation, Writing – Original Draft, Visualization. Leo Kriegsman: Validation, Methodology, Data Curation, Writing – Review and Editing, Supervision. Barbara Kunz: Methodology, Resources, Validation, Writing – Review and Editing, Supervision. Clare Warren: Writing – Review and Editing, Supervision, Project administration, Funding acquisition. Tom Argles : Writing – Review and Editing, Supervision.

Data availability Data is provided within the manuscript or supplementary information files.

Declarations

Competing interests The authors declare no competing interests.

References

Antona J, Fallick A, Sanchez G (1994) Fluid-inclusion and stable-isotope studies of gold-tungsten bearing hydrothermal deposits, Saucelle-Barruecopardo area, Spain. Eur J Mineral 6(6):819–835

Aumar C, Merle O, Bosse V, Monié P (2022) Syn-rift cretaceous deformation in the Agly variscan Massif (Eastern Pyrenees, France). BSGF - Earth Sci Bull 193:6

Baidya AS, Pal DC, Upadhyay D (2019) Chemical weathering of Garnet in banded iron formation: implications for the mechanism and sequence of secondary mineral formation and mobility of elements. Geochim Cosmochim Acta 265:198–220

Bertoldi C, Proyer A, Garbe-Schönberg D, Behrens H, Dachs E (2004) Comprehensive chemical analyses of natural cordierites: implications for exchange mechanisms. Lithos 78(4):389–409

Broussolle A, Štípská P, Lehmann J, Schulmann K, Hacker BR, Holder R, Kylander-Clark ARC, Hanžl P, Racek M, Hasalová P, Lexa O (2015) P–T–t–D record of crustal-scale horizontal flow and magma-assisted doming in the SW Mongolian Altai. J Metamorph Geol 33(4):359–383

Brown M (1975) The petrogenesis of the St. Malo migmatite belt, North-Eastern Brittany, France. Doctoral Dissertation, University of Keele

Caldevilla P, González-Menéndez L, Martín-Crespo T, Vindel E, Guedes A, Berrezueta E, Castañón AM, Gómez-Fernández F (2023) The Peña do Seo W-Sn deposit, NW iberia: petrology, fluid inclusions and O-H-S isotopes. Ore Geol Rev 155:105361

Cathelineau M, Boiron M-C, Marignac C, Dour M, Dejean M, Carocci E, Truche L, Pinto F (2020) High pressure and temperatures during the early stages of tungsten deposition at Panasqueira revealed by fluid inclusions in Topaz. Ore Geol Rev 126:103741

Chen S-C, Yu J-J, Zhao X-F, Bi M-F, Lehmann B (2023) Various chlorite alteration styles in the furong Sn deposit, South china: chlorite chemistry and implication for Tin mineralization. Ore Geol Rev 162:105680

Deer WA, Howie RA, Zussman J (2013) An introduction to the rock-forming minerals. Mineralogical Society of Great Britain and Ireland, London

Eggleton RA, Banfield JF (1985) The alteration of granitic biotite to chlorite. Am Mineral 70(9–10):902–912

Faehnrich K, Kośmińska K, Majka J (2023) Mass transfer and element redistribution during chloritization of metamorphic biotite in a metapelite: insights from compositional mapping. Mineralogia 54:1–22

Finger F, Clemens JD (1995) Migmatization and secondary granitic magmas: effects of emplacement and crystallization of primary granitoids in Southern Bohemia, Austria. Contrib Mineral Petrol 120(3):311–326

Finger F, Roberts MP, Haunschmid B, Schermaier A, Steyrer HP (1997) Variscan granitoids of central europe: their typology, potential sources and tectonothermal relations. Mineral Petrol 61(1–4):67–96

Franke W, Ballèvre M, Cocks LRM, Torsvik TH, Żelaźniewicz A (2021) Variscan orogeny. In: Alderton D, Elias S (eds) Encyclopedia of geology, 2nd edn. Academic, pp 338–349

Fuhrman ML, Lindsley DH (1988) Ternary-feldspar modeling and thermometry. Am Mineral 73(3–4):201–215

Holland TJB, Powell R (2011) An improved and extended internally consistent thermodynamic dataset for phases of petrological interest, involving a new equation of state for solids. J Metamorph Geol 29(3):333–383

Hoyer M, Kummer N-A, Merkel B (2015) Sorption of lithium on bentonite, Kaolin and zeolite. Geosciences 5(2):127–140

Hövelmann J, Putnis A, Geisler T Golla-Schindler U (2010) The replacement of plagioclase feldspars by albite: observations from hydrothermal experiments. Contrib Mineral Petrol 159:43–59

Jennings ES, Holland TJB (2015) A simple thermodynamic model for melting of peridotite in the system NCFMASOCr. J Petrol 56(5):869–892

Ji Y, Hennissen JAI, Hough E, Vandeginste V (2021) Geochemical element mobilisation by interaction of Bowland shale with acidic fluids. Fuel 289:119914

Johnson T, Brown M (2004) Quantitative constraints on metamorphism in the variscides of Southern Brittany—a complementary pseudosection approach. J Petrol 45(6):1237–1259

Kunz B, Warren C, Jenner F, Harris N, Argles T (2022) Critical metal enrichment in crustal melts: the role of metamorphic mica. Geology 50(11):1219–1223

Lal RK (1969) Retrogression of cordierite to kyanite and Andalusite at fishtail Lake, Ontario, Canada. Mineral Mag 37(288):466–471

Lanari P, Wagner T, Vidal OA (2014) Thermodynamic model for di-trioctahedral chlorite from experimental and natural data in the system MgO–FeO–Al2O3–SiO2–H2O: applications to P–T sections and geothermometry. Contrib Mineral Petrol 167:968

Li J, Zhang W, Li S, Li X, Lu J (2014) Effects of citrate on the dissolution and transformation of biotite, analyzed by chemical and atomic force microscopy. Appl Geochem 51:101–108

Liu X, Yu P, Xiao C (2023) Tin transport and cassiterite precipitation from hydrothermal fluids. Geosci Front 14(6):101624

López-Moro FJ, López-Plaza M, Romer RL (2012) Generation and emplacement of shear-related highly mobile crustal melts: the synkinematic leucogranites from the variscan tormes Dome, Western Spain. Int J Earth Sci 101(5):1273–1298

Ludhová L, Janák M (1999) Phase relations and PT path of cordierite bearing migmatites, Western Tatra Mountains, Western Carpathians. Geol Carpath 50(4):283–293

Luvizotto GL, Zack T, Meyer HP, Ludwig T, Triebold S, Kronz A, Münker C, Stockli DF, Prowatke S, Klemme S, Jacob DE, von Eynatten H (2009) Rutile crystals as potential trace element and isotope mineral standards for microanalysis. Chem Geol 261(3–4):346–369

Mei Y, Liu W, Guan Q, Brugger J, Etschmann B, Siegel C, Wykes J, Ram R (2025) Tungsten speciation in hydrothermal fluids. Geochim Cosmochim Acta 406:262–284

Moine B, Fortune JP, Moreau P, Viguier F (1989) Comparative mineralogy, geochemistry, and conditions of formation of two metasomatic Talc and chlorite deposits; Trimouns (Pyrenees, France) and Rabenwald (Eastern Alps, Austria). Econ Geol 84(5):1398–1416

Monnier L, Salvi S, Melleton J, Lach P, Pochon A, Bailly L, Béziat D, De Parseval P (2022) Mica trace-element signatures: highlighting superimposed W-Sn mineralizations and fluid sources. Chem Geol 600:120866

Neiva AMR (2008) Geochemistry of cassiterite and wolframite from Tin and tungsten quartz veins in Portugal. Ore Geol Rev 33(3–4):221–238

Noronha F (2017) Fluids and variscan metallogenesis in granite related systems in Portugal. Procedia Earth Planet Sci 17:1–4

Noronha F, Doria A, Dubessy J, Charoy B (1992) Characterization and timing of the different types of fluids present in the barren and ore-veins of the W-Sn deposit of Panasqueira, central Portugal. Min Depos 27(1):72–88

Novák M, Gadas P, Filip J, Vaculovič T, Přikryl J, Fojt B (2011) Blue, complexly zoned, (Na,Mg,Fe,Li)-rich Beryl from quartz-calcite veins in low-grade metamorphosed Fe-deposit Skály near Rýmařov, Czech Republic. Mineral Petrol 102(1–4):3–14

Ogiermann JC (2002) Cordierite and its retrograde breakdown products as monitors of fluid-rock interaction during retrograde path metamorphism: case studies in the Schwarzwald and the Bayerische Wald (Variscan belt, Germany). Doctoral dissertation, Ruperto-Carola University of Heidelberg

Osvald M, Kilpatrick AD, Rochelle CA, Szanyi J, Medgyes T, Kobor B (2018) Laboratory leaching tests to investigate mobilisation and recovery of metals from geothermal reservoirs. Geofluids 2018(1):6509420

Oziegbe EJ, Oziegbe O (2023) Retrograde assemblages of gneisses at arigidi and Erusu areas of Southwestern Nigeria. IOP Conf Ser Earth Environ Sci 1197:012010

Paton C, Hellstrom J, Paul B, Woodhead J, Hergt J (2011) Iolite: freeware for the visualisation and processing of mass spectrometric data. J Anal Spectrom 26(12):2508–2518

Perreault S, Martignole J (1988) High temperature cordierite migmatites in the North Eastern Grenville Province. J Metamorph Geol 6(6):673–696

Putnis A (2021) Fluid–mineral interactions: controlling coupled mechanisms of reaction, mass transfer and deformation. J Petr 62(12)

Romer RL, Kroner U (2016) Phanerozoic Tin and tungsten mineralization—tectonic controls on the distribution of enriched protoliths and heat sources for crustal melting. Gondwana Res 31:60–95

Sanjuan B, Gourcerol B, Millot R, Rettenmaier D, Jeandel E, Rombaut A (2022) Lithium-rich geothermal Brines in europe: an up-date about geochemical characteristics and implications for potential Li resources. Geothermics 101:102385

Silva MA (2014) Petrogenesis of a variscan migmatite complex (NW Portugal): petrography, geochemistry and fluids. Doctoral Dissertation, Universidade do Porto

Sinclair WD, Gonevchuck GA, Korostelev PG, Semenyak BI, Rodlonov S, Seltmann R, Stemprok M (2011) World distribution of Tin and tungsten deposits. Geological Survey of Canada. Open File, 5482, Natural Resources Canada

Siron G, Goncalves P, Marquer D, Pierre T, Paquette J-L, Vanardois J (2020) Contribution of magmatism, partial melting buffering and localized crustal thinning on the late variscan thermal structure of the Agly Massif (French Pyrenees). J Metamorph Geol 38(8):799–829

Åström ME, Yu C, Peltola P, Reynolds JK, Österholm P, Nystrand MI, Augustsson A, Virtasalo JJ, Nordmyr L, Ojala AEK (2018) Sources, transport and sinks of beryllium in a coastal landscape affected by acidic soils. Geochim Cosmochim Acta 232:288–302

Sturm R (2017) Cordierite from a high-temperature low-pressure shear zone of the south-western Bohemian Massif (Moldanubian terrain, Austria). Geochem 77(1):195–206

Tartèse R, Boulvais P, Poujol M, Chevalier T, Paquette J-L, Ireland TR, Deloule E (2012) Mylonites of the South Armorican shear zone: insights for crustal-scale fluid flow and water–rock interaction processes. J Geodyn 56–57:86–107

Thompson JB Jr (1982) Composition space; an algebraic and geometric approach. Rev Mineral Geochem 10(1):1–31

Viruete JE, Indares A, Arenas R (2000) P–T paths derived from Garnet growth zoning in an extensional setting: an example from the tormes gneiss dome (Iberian Massif, Spain). J Petrol 41(10):1489–1515

Walker JR (1993) Chlorite polytype geothermometry. Clays Clay Min 41(2):260–267

Walter BF, Kortenbruck P, Scharrer M, Zeitvogel C, Wälle M, Mertz-Kraus R, Markl G (2019) Chemical evolution of ore-forming brines – basement leaching, metal provenance, and the redox link between barren and ore-bearing hydrothermal veins. A case study from the Schwarzwald mining district in SW-Germany. Chem Geol 506:126–148

Watson EB, Wark DA, Thomas JB (2006) Crystallization thermometers for zircon and rutile. Cont Min Petr 151(4):413–433

White RW, Powell R, Holland TJB, Johnson TE, Green ECR (2014) New mineral activity–composition relations for thermodynamic calculations in metapelitic systems. J Metamorph Geol 32(3):261–286

Whitney DL, Evans BW (2010) Abbreviations for names of rock-forming minerals. Am Mineral 95(1):185–187

Wu CM, Chen HX (2015) Revised Ti-in-biotite geothermometer for ilmenite-or rutile-bearing crustal metapelites. Scie Bull 60(1):116–121

Xiang H, Connolly JAD (2022) GeoPS: an interactive visual computing tool for thermodynamic modelling of phase equilibria. J Metamorph Geol 40(2):243–255

Xie L, Wang R-C, Chen J, Zhu J-C (2010) Mineralogical evidence for magmatic and hydrothermal processes in the Qitianling oxidized tin-bearing granite (Hunan, South China): EMP and (MC)-LA-ICPMS investigations of three types of titanite. Chem Geol 276(1–2):53–68

Yang Z-Y, Wang R-C, Che X-D, Harlov D (2023) Restrictions on Niobium enrichment by alteration of Niobium-rich biotite in pure water, acid, alkaline and fluoride-bearing solutions at 200 MPa and 300–600°C. Geochim Cosmochim Acta 343:115–132

Yang Z-Y, Wang R, Che X, Yin R, Xie L, Hu H (2020) Formation of columbite and microlite after alteration of Nb- and Ta-bearing biotite from the Lizaizhai pegmatite (Guangning ore district, Guangdong, South China): identification of a new potential Nb–Ta mineralization type. J Asian Earth Sci 190:104154

Yardley BWD, Rhede D, Heinrich W (2014) Rates of retrograde metamorphism and their implications for the rheology of the crust: an experimental study. J Petr 55(3):623–641

Yuan J, Hou Q, Yang Z, Jiang H, Hu Z, Yu T (2018) Distribution and mobilization of Sn in silicate minerals from the mesozoic Shizhuyuan W-dominated polymetallic deposit, South China. Ore Geol Rev 101:595–608

Yuan X, Hu Y, Zhao Y, Li Q, Liu C (2021) Contribution of hydrothermal processes to the enrichment of lithium in brines: evidence from water–rock interacting experiments. Aquat Geochem 27(3):221–239

Zhang J-Y, Wang Q, Liu X-F, Zhou G-F, Xu H-P, Zhu Y-G (2022) Provenance and ore-forming process of permian lithium-rich bauxite in central Yunnan, SW China. Ore Geol Rev 145:104862

Zhao H, Ling K, Qin S, Lei M, Wen H (2023) Modes of occurrence of lithium in black shale in the Nandan area, Guangxi, SW china: implications for clay-type resources. Ore Geol Rev 157:105409